



#### Available online at www.sciencedirect.com

# **ScienceDirect**

Comput. Methods Appl. Mech. Engrg. 362 (2020) 112781

Computer methods in applied mechanics and engineering

www.elsevier.com/locate/cma

# FFT-based solver for higher-order and multi-phase-field fracture models applied to strongly anisotropic brittle materials

Ran Ma, WaiChing Sun\*

Department of Civil Engineering and Engineering Mechanics, Columbia University, 614 SW Mudd, Mail Code: 4709, New York, NY 10027, United States of America

Received 30 May 2019; received in revised form 12 November 2019; accepted 5 December 2019

Available online xxxx

#### **Abstract**

This paper presents the application of a fast Fourier transform (FFT) based method to solve two phase field models designed to simulate crack growth of strongly anisotropic materials in the brittle regime. By leveraging the ability of the FFT-based solver to generate solutions with higher-order and global continuities, we design two simple algorithms to capture the complex fracture patterns (e.g. sawtooth, and curved crack growth) common in materials with strongly anisotropic surface energy via the multi-phase-field and high-order phase-field frameworks. A staggered operator-split solver is used where both the balance of linear momentum and the phase field governing equations are formulated in the periodic domain. The unit phase field of the initial failure region is prescribed by the penalty method to alleviate the sharp material contrast between the initial failure region and the base material. The discrete frequency vectors are generalized to estimate the second and fourth order gradients such that the Gibbs effect near shape interfaces or jump conditions can be suppressed. Furthermore, a preconditioner is adopted to improve the convergence rate of the iterative linear solver. Three numerical experiments are used to systematically compare the performance of the FFT-based method in the multi-phase-field and high-order phase-field frameworks.

© 2019 Elsevier B.V. All rights reserved.

Keywords: Fast Fourier transform; Multi-phase-field fracture; Higher-order phase field fracture; Anisotropic cracks; Polycrystal; Salt

# 1. Introduction

The variational approach to fracture has provided a new way to simulate crack evolution in a purely elastic deforming body by finding the deformation field and evolving crack paths that minimizes an energy functional [1,2]. This approach is well suited for phase field models which represent sharp interfaces with via implicit functions [3–13]. While thermodynamically consistent formulations are proposed by Miehe et al. [3], a material-force-based formulation of phase field model has been derived and tested as an alternative way to introduce phase field fracture models (e.g. Borden et al. [14,15], Choo and Sun [16]).

Unlike the embedded discontinuity approach such as assumed strain (e.g. Regueiro and Borja [17], Wang and Sun [18,19,20]), extended/generalized finite element (e.g. Moës et al. [21], Duarte et al. [22], Sun et al. [23]) and strong-discontinuity surface element (e.g. Ortiz and Pandolfi [24], Linder and Raina [25], Radovitzky et al. [26]), the

E-mail address: wsun@columbia.edu (W. Sun).

<sup>\*</sup> Corresponding author.

phase field fracture method does not explicitly capture the jump condition with an enhanced basis for displacement. Instead, a continuous phase field is used to indicate the location of the damaged zone that may be interpreted as the diffusive approximation of the jump conditions. While this approximated condition may not capture the evolving geometry of the crack exactly, the introduction of the continuous field provides a simple way to simulate crack growth without predefined crack propagation paths, allows the simulations of crack coalescence and interaction and branching without the need of ad hoc branching algorithm and enables one to explicitly define crack nucleation rule as a driving force.

Recent work, such as Clayton and Knap [27], Bryant and Sun [9], Quintanas-Corominas et al. [28], has extended the phase field model to capture brittle fracture in anisotropic materials where the surface energy depends on the orientation of the crack propagation direction [27], the fracture mode [9] and the mechanism of rupture of fiber in composite [28]. The modification of the phase field model is relatively simple when the surface energy remains convex. However, a complex microstructure may lead to strongly anisotropic surface energy that is concave and cannot be described via a second-order structural tensor. Furthermore, solving this strongly anisotropic phase field fracture is difficult for second-order finite element method with traditional polynomial basis. Recent work has resolved this issue in a finite element framework by either introducing multiple phase fields or employing finite element space spanned by isogeometric basis to preserve higher-order continuity across finite elements. In the former case, the introduction of multiple phase field does not require significant changes in the finite element models and is therefore convenient. Furthermore, the multi-phase-field formulation also provides modelers a simple mechanism to incorporate different driving forces and degradation mechanisms. As the total free energy can be any non-negative-valued function of deformation and the multiple phase fields, this approach provides the great flexibility to evolve anisotropic damages as shown in [7,29,30]. Nevertheless, the multi-phase-field formulation also unavoidably leads to the extra degrees of freedoms and a sizable increase of computational demand [7,27,29,30]. This increase in computational demand is significant, given the high spatial resolution demanded for fracture simulations.

Alternatively, a fourth-order isogeometric approach has been introduced in previous works, such as Teichtmeister et al. [31], Borden et al. [14]. In this case, the strongly anisotropic surface energy of a brittle material can be captured with a single phase field since one may choose the isogeometric basis of arbitrary continuity. The use of isogeometric basis is particularly convenient for a design workflow that involves computer-aided design where the isogeometric analysis and the design software may employ the same set of basis functions [23,32,33]. However, the higher-order continuity may also lead to a denser tangential matrix that may slow down the speed of an implicit iterative solver even if a pre-conditioner is used.

#### 1.1. Rationales of using FFT solver for resolving strongly anisotropic brittle materials

The FFT-based method, an algorithm first introduced in Moulinec and Suquet [34] to solve elasticity and inelasticity problems via Fast Fourier Transform, is an efficient alternative to solve the anisotropic phase field problems for brittle materials exhibiting strongly anisotropic surface energy in a periodic unit cell. Due to the usage of the Fourier space, an FFT-based solver can easily solve problems that involve higher-order derivatives. Furthermore, it also does not require the generation of a suitable mesh as it can be simply solved in a Cartesian grid. This feature makes the FFT-solver a very feasible choice for solving elasticity problems for heterogeneous materials with spatial properties discretized by pixels or voxels. Finally, the implementation of an FFT-based solver is relatively simple. A simple implementation is often completed within ten lines of code [35]. This combination of desirable traits makes the FFT-based solver an attractive option for resolving anisotropic phase field fracture problems in unit cells where the formulation demands high resolutions, sufficient continuity, and computational efficiency.

Such an FFT solver is not only useful for simulations in periodic unit cells, but can be used for multiscale simulations that are based on computational homogenization (e.g. Feyel [36], Sun et al. [37], Sun et al. [38], Liu et al. [39], Shahin et al. [40], Wang and Sun [18]), and global–local formation for phase field fracture or gradient damage models (cf. Wu et al. [41], Noii et al. [12]).

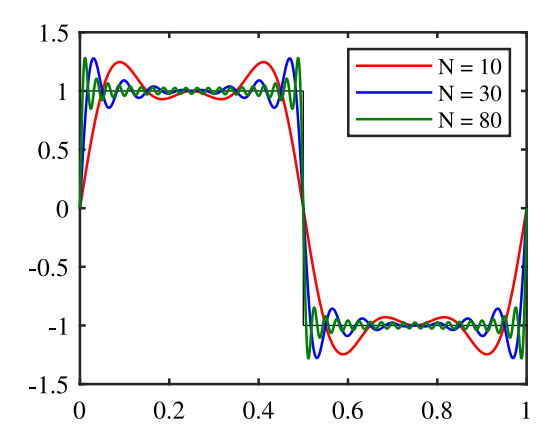


Fig. 1. Fourier series approximation of a square wave. N is the number of terms used to approximate the square wave. Gibbs phenomenon occurs when the Fourier series overshoot at the sharp discontinuities and cause spurious oscillations.

#### 1.2. Literature review on FFT-based solvers

The FFT-based method was first proposed to solve linear elastic inclusion problems by utilizing the Lippmann-Schwinger equation defined on a periodic homogeneous reference material [34,42]. This original algorithm, which uses point collocation and truncation of Fourier series to iterate between the Fourier and real space, is often referred to as the basic scheme. Based upon this basic scheme, an accelerated scheme [43] and an augmented-Lagrangian scheme [44] are independently proposed to improve the accuracy, efficiency and robustness of the FFT solvers that deal with materials exhibiting jumps or sharp gradient in material properties. In the last two decades, significant improvements of the FFT solver have been achieved such that they enable the applications of the FFT-based solver for high-resolution simulations performed on complex microstructure and 3D images of a wide spectrum of materials, such as polycrystals [45-47] and composite materials [48]. Nevertheless, since FFT solver employs trigonometric polynomials as the basis function of the solution, spurious oscillations may occur when a jump condition is being approximated by the Fourier series of piecewise continuous differentiable functions. This spurious oscillation is often referred to as the Gibbs phenomenon or Gibbs effect Since the Gibbs phenomenon is caused by the Fourier sums overshooting at a jump condition, and the decay of the Fourier coefficient at infinity is controlled by the smoothness, a sharp gradient or jump is difficult to approximate even though the number of terms significantly increase, as shown in Fig. 1. Special numerical treatments are therefore required to dampen the Gibbs effect if the solution field is expected to include sharp gradient (e.g. regularized phase field for fracture).

Notwithstanding the advantages the FFT-based methods have on material failure problems, the corresponding applications on solving damage mechanics problems have not been attempted until recently. For instance, Li et al. [49] and Boeff et al. [50] have both use FFT solvers to simulate damage of materials characterized by the integral based damage model (cf. Li et al. [49]) and the gradient-based damage model (cf. Boeff et al. [50]). These examples indicate that the FFT solver is well suited to simulate damage with regularization enabled by both nonlocal integral and gradient dependence. A similar procedure has also been applied to simulate the failure of composite materials (e.g. Wang et al. [51]) as well as the interface decohesion problem in which the cohesive zone model was solved by introducing length scale contrast between the interphase region and the bulk region [52]. Finally, the FFT-based damage mechanics solver has also been incorporated in a multiscale homogenization framework to model brittle fracture of composite materials across length scales [53]. The successful application of the FFT-based method on continuum damage mechanics indicates its potential to solve phase-field brittle fracture problems, where the crack is explicitly represented with  $\Gamma$ -convergence to the critical energy release rate for Griffith's theory. Although high material contrast exists between the damaged region and the intact region, it is shown that the FFT-based method produces similar results as the FE method regarding the crack tip stress field without suffering from the Gibbs phenomenon [49,54].

FFT-based spectral method has been used to solve both the Ginzburg-Landau equation and Cahn-Hilliard equation for interface migration problems in a semi-implicit fashion [55]. In these formulations, the phase field

governing equations are assumed to be isotropic and homogeneous. The similar numerical technique was employed recently to simulate dynamic re-crystallization [56] and martensite—austenite transformation [57]. Recently, FFT-based method was employed to solve phase-field fracture problem in both small strain elasticity case [58] and finite strain elasto-plasticity case [59].

Despite the great potential of the FFT solver to capture strongly anisotropic brittle fracture for materials of complex microstructures, there is not yet any attempt to incorporate FFT solver to simulate phase field fractures for anisotropic materials. This might be attributed to the facts that (1) FFT-based solver may suffer from slow convergence if sharp material contract, such as bi-material interfaces, void and cavity, is presented in the spatial domain [60], and (2) one must resolve the higher order gradient required for collocation method while circumventing the Gibbs phenomena that leads to spurious oscillations near crack tip or other locations that exhibit sharp gradients.

#### 1.3. Objectives and organization of contents

The purpose of this paper is to introduce a mathematical framework that overcomes the aforementioned obstacles such that the fractures of materials with strongly anisotropic energy can be resolved via an FFT solver. To close this knowledge gap, we successfully build two FFT solvers, i.e. one for the multi-phase-field fracture model (which does not require higher-order continuity but introduce additional field variables), and another one for the higher-order phase field fracture model (which requires only one phase field but requires higher-order continuity). The strength and weakness of both modeling approaches in the FFT setting are analyzed and compared in numerical experiments.

Note that representing the initial flaw using the so-called gas phase with zero stiffness may introduce sharp material contrast that deteriorates the convergence rate of the FFT-based solver. To avoid this issue, we introduce a formulation such that inclusions, cavities or initial flaws can be represented as Dirichlet-type boundary conditions weakly enforced by the penalty method.

To overcome the well-known Gibbs effect exhibited in the solution obtained via FFT solver, which leads to spurious high-frequency oscillations at the location where sharp material contrast presents, we approximate the continuum frequency vector via a generalized version of the finite-difference based frequency operator first introduced in Berbenni et al. [61], Willot et al. [62], Schneider et al. [63] to calculate second- and fourth-order gradient while avoiding numerical instability. The discretized governing equation is then solved at each grid point via a matrix-free iterative linear solver. Three numerical examples are presented to compare the numerical performance of the multi-phase-field model and the high-order phase-field model. Meanwhile, an interface damage model is proposed to capture the path-dependent responses of material interfaces.

This paper will proceed as follows. Section 2 discusses the governing equation and the numerical solution of multi-phase-field and high-order phase-field, respectively. Also, an interface failure model is proposed in to represent material interface failure, for example grain boundary crack and fiber-polymer de-cohesion. In Section 3, three examples are presented to compare the convergence rate and the numerical performance of the multi-phase-field and the high-order phase field. Section 4 summarizes the major results and concluding remarks.

As for notations and symbols, bold-faced letters denote tensors (including vectors which are rank-one tensors); the symbol '·' denotes a single contraction of adjacent indices of two tensors (e.g.  $a \cdot b = a_i b_i$  or  $c \cdot d = c_{ij} d_{jk}$ ); the symbol ':' denotes a double contraction of adjacent indices of tensor of rank two or higher (e.g.  $C : e^e = C_{ijkl} e_{kl}^e$ ); the symbol '::' denotes a fourth contraction of adjacent indices of tensor of rank four or higher (e.g.  $C : D = C_{ijkl} D_{ijkl}$ ); the symbol 'S' denotes a juxtaposition of two vectors (e.g.  $a \otimes b = a_i b_j$ ) or two symmetric second order tensors (e.g.  $a \otimes b = a_i b_j$ ); the symbol 'F' and 'F<sup>-1</sup>' represent forward and backward Fourier transformation, respectively. Materials are assumed to be simple cubic symmetry throughout this paper unless specified.

#### 2. Strongly anisotropic phase field theories

In this section, we review the two most common phase field models, i.e., the multi-phase-field model and the higher-order phase field model, used to replicate crack growth of materials with strongly anisotropic surface energy and introduce a modified version of phase field model designed to capture fractures and damage across interfaces and/or grain boundaries. The following assumptions are made in both models:

- 1. The inertial effects are negligible.
- 2. The material is under the isothermal condition.

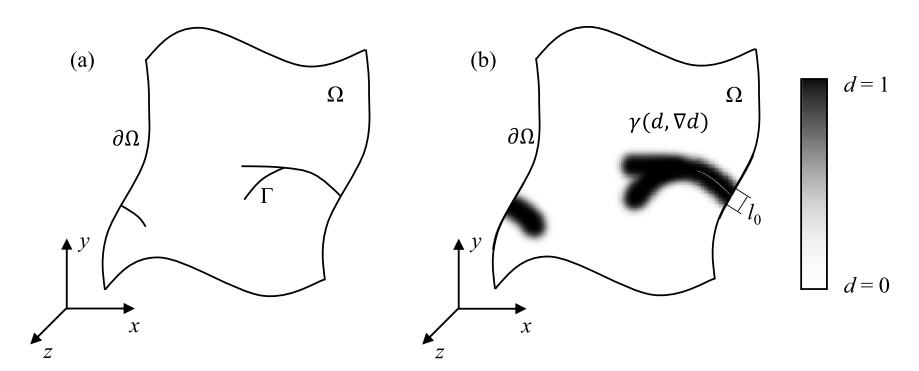


Fig. 2. A schematic demonstration of phase field fracture in the deformed configuration of RVE subjected to periodic boundary condition.

(a) A solid body with sharp crack; (b) A solid body with regularized crack.

- 3. Rate dependence is neglected.
- 4. The deformation is infinitesimal such that the effect of geometrical nonlinearity can be neglected.
- 5. The boundary conditions are periodic.
- 6. The material is either elastic or in the brittle fracture regimes.

In addition, we consider a general case in which the surface energy can be non-convex. In the case of the multiphase field model, we follow the treatment in Nguyen et al. [29] and Na and Sun [7,64] such that the strongly anisotropic brittle fracture is manifested by using multiple phase fields, each phase field is associated with damage accumulated on the corresponding plane orthogonal to a pre-defined normal vector. In the case of the high-order phase field, the governing equation of the phase field is modified to incorporate the higher-order terms such that the nonconvex surface energy can be characterized. Both phase field models are solved via a fast Fourier transform solver (cf. Zeman et al. [60], Ma and Truster [47], Eghtesad et al. [65]). As a result, the spatial domain of the boundary value problem is idealized as a unit cell subjected to periodic boundary conditions. This unit cell, denoted as  $\Omega$  herein, represents a microstructure discretized by cubic voxels whose centroids are FFT points in a regular Cartesian grid, as shown in Fig. 2. Meanwhile, the periodic boundary conditions provide a mean for us to employ solution space spanned by the trigonometric basis functions, while also generates homogenized responses that are bounded by both the traction- and displacement-based boundary conditions [37–39,66–69]. The crack surface is denoted as  $\Gamma$ . As such, the total energy potential within the cracked body can be decomposed into the elastic stored energy and the free surface energy:

$$\Psi = \int_{\Omega} \psi_e d\Omega + \int_{\Gamma} G_c d\Gamma, \tag{1}$$

where  $\psi_e$  is the elastic strain energy density, and  $G_c$  is the cleavage energy per unit area.

In the phase field brittle fracture theory, the sharp crack surface  $\Gamma$  is represented by a diffusive regularized implicit indicator function called phase field (denoted as d herein), where d=0 represents the intact region and d=1 represents the completely damaged region [2,5,6,9,70,71]. This damage phase field d is regularized such that the infinitesimal unit surface area  $d\Gamma$  is smeared to an infinitesimal domain  $\gamma d\Omega$ , as shown in Fig. 2(b), and the total cleavage energy can be approximated by domain integral:

$$\lim_{l_0 \to 0} \int_{\Omega} G_c \gamma (d, \nabla d) d\Omega = \int_{\Gamma} G_c d\Gamma, \tag{2}$$

where  $l_0$  is the regularization length scale. The strongly anisotropic phase field theory can be introduced by using an anisotropic non-convex crack surface density  $\gamma$  in two approaches. The first approach uses multiple phase fields with each phase field representing one preferential crack propagation direction [27]. The second approach uses one phase field with high order gradient terms [31].

In this section, a multi-phase-field based small strain elasticity model is first introduced, which provides the driving force for both multi-phase-field and high-order phase-field. Then the multi-phase-field theory and high-order phase-field theory are derived in a periodic unit cell, with the governing equations solved by the FFT-based method. Also, an interface model is presented to accommodate both phase field theories.

#### 2.1. Small strain isotropic elasticity

The strain free energy  $\psi_e$  in Eq. (1) is a function of the mechanical constitutive relation. The classical isotropic linear elasticity model is used to replicate the elastic responses. This approximation is acceptable for crystalline materials such as rock salt which does not exhibit strong anisotropy in the elastic regime [72,73]. Meanwhile, we assume that the surface energy for the fracture is of cubic symmetry for both multi-phase-field and high-order phase-field, which is suitable for crystalline materials which exhibits four three-fold rotational axes oriented at  $109.5^{\circ}$  with respect to each other. The elastic strain energy reads:

$$\psi_e(\boldsymbol{\varepsilon}, d) = \frac{1}{2} \kappa \varepsilon_v^2 + \mu \left( \boldsymbol{\varepsilon} : \boldsymbol{\varepsilon} - \frac{1}{3} \varepsilon_v^2 \right). \tag{3}$$

Here,  $\varepsilon_v$  is the volumetric strain  $\varepsilon_v = \operatorname{tr}(\boldsymbol{\varepsilon})$ , and  $\kappa$  and  $\mu$  are the Lamé constants.

The total material degradation D at point x is defined as:

$$D = k + (1 - k) \prod_{i=1}^{n} (1 - d_i)^2,$$
(4)

where  $k \ll 1$  is a small portion of the residual stiffness to retain well-posedness, n is the total number of phase fields, and  $d_i$  is the i th damage phase field. Assume, without loss of generality, that n > 1 for multi-phase-field and n = 1 for high-order phase-field throughout this paper. Then for the multi-phase-field method (n > 1), each phase field  $d_i$  is corresponding to the damage along a preferential propagation direction, following the treatment in Nguyen et al. [29], Na and Sun [7]. The Lamé constants  $\kappa$  and  $\mu$  are functions of the local damage phase field:

$$\mu(d) = D\mu_0, \quad \kappa(d) = \begin{cases} \kappa_0 & , & \varepsilon_v \le 0 \\ D\kappa_0 & , & \varepsilon_v > 0 \end{cases}$$
 (5)

where  $\kappa_0$  and  $\mu_0$  are the undamaged Lamé constants. Note that the elastic constitutive relation is anisotropic in that the volumetric modulus  $\kappa$  depends on the current volumetric strain  $\varepsilon_v$ . The strain energy functional for the i th phase field within totally n number of phase fields is defined as:

$$\mathcal{H}_{n}^{i} = (1 - k) \max_{\tau \in [0, t]} \left\{ \prod_{j=1, j \neq i}^{n} \left( 1 - d_{j} \right)^{2} \left[ \frac{1}{2} \kappa_{0} \langle \varepsilon_{v} \rangle^{2} + \mu_{0} \left( \boldsymbol{\varepsilon} : \boldsymbol{\varepsilon} - \frac{1}{3} \varepsilon_{v}^{2} \right) \right] \right\}, \tag{6}$$

where  $\langle \cdot \rangle := (\cdot + |\cdot|)/2$ . For multi-phase-field, n is a positive integer, while for high-order phase field n equal to one. In this equation, the monotonically increasing of damage is enforced by using the maximum strain energy functional in time  $\tau \in [0, t]$  to form the energy functional for the variational problem. The corresponding thermodynamic driving force associated to  $d_i$  reads (cf. Nguyen et al. [29]),

$$F_i = (1 - d_i)\mathcal{H}_n^i - G_c\delta\gamma_i(d_i, \nabla d_i) = 0 \tag{7}$$

where the second term in Eq. (7) is the thermodynamic force related to the growth of the phase field  $d_i$ .

#### 2.2. Multi-phase-field model

In multi-phase-field theory, the total cleavage energy is split to multiple anisotropic cleavage energies, each represented by a separate phase field  $d_i$ :

$$\int_{\Omega} G_c \gamma d\Omega = \int_{\Omega} G_c \sum_{i=1}^{n} \gamma_i(d_i, \nabla d_i) d\Omega.$$
(8)

In this way, the total cleavage energy is non-convex and can be applied to simulate strongly anisotropic brittle fracture.

#### 2.2.1. Phase field theory in periodic unit cell

Crack density per unit volume  $\gamma_i$  is defined as a function of the damage phase field and its gradient:

$$\gamma_i(d_i, \nabla d_i) = \sum_{i=1}^n \left[ \frac{1}{2l_0} d_i^2 + \frac{l_0}{2} \nabla d_i \cdot A_i \cdot \nabla d_i + \frac{1}{2} \beta_p (d_i - 1)^2 \right], \quad d_i \in H^1_{\#}(\Omega),$$
(9)

where  $l_0$  is the regularization length scale, A is the second order anisotropic tensor, and  $\beta_p$  is the penalty parameter to enforce the phase field within the initial damage region. Function space  $H^p_\#(\Omega)$  is the space of all periodic functions with p th order square integrable weak gradient. The anisotropic tensor A is usually formulated as:

$$A_i = [I + \beta_{ma} (I - \mathbf{n}_i \otimes \mathbf{n}_i)], \tag{10}$$

where  $n_i$  is the normal direction of the preferential crack propagation direction corresponding to the *i* th phase field, I is the second order identity tensor. The penalty parameter  $\beta_{ma}$  serves to penalize the anisotropic propagation, where  $\beta_{ma} = 0$  recovers the isotropic phase field theory.

Total crack surface area  $\Gamma$  in the unit cell  $\Omega$  is defined as the domain integration of the crack surface density  $\gamma$ :

$$\Gamma_i(d) = \int_{\Omega} \gamma_i (d_i, \nabla d_i) \, \mathrm{d}\Omega, \tag{11}$$

which is a functional that depends on the damage phase field d and its gradient. The initial balanced phase field distribution  $d_i(t=0)$  minimizes the total crack surface energy:

$$d_i(\mathbf{x}) = \operatorname{Arg} \left[ \inf_{d_i \in H_{\#}^1(\Omega)} \Gamma_l(d_i, \nabla d_i) \right]. \tag{12}$$

The current equilibrium mechanical field and damage field shall minimize the total potential  $\Psi$  defined in Eq. (1), where the elastic strain energy  $\psi_e$  is defined in (3) and the crack surface density  $\gamma$  is defined in (9). Therefore, the first order variation of the total potential functional should vanish, which is a necessary condition of total potential stationary condition. The mechanical part of the variational equations yields the equilibrium equation

$$\nabla \cdot \boldsymbol{\sigma} = \boldsymbol{0},\tag{13}$$

where the body force is neglected. Then, the i th phase field distribution can be determined such that the first order variation with respect to  $d_i$  vanishes:

$$\int_{\Omega} \left[ 2(d_i - 1)\mathcal{H}_n^i \delta d_i + G_c \left( \frac{d_i}{l_0} \delta d_i + l_0 \nabla d_i \cdot A_i \cdot \nabla \delta d_i + \beta_p \left( d_i - 1 \right) \delta d_i \right) \right] d\Omega = 0, \ \forall \delta d_i \in H_{\#}^1, \tag{14}$$

which holds for arbitrary phase field perturbation  $\delta d_i$  in the  $H^1_{\#}$  space. Note that the FFT approach is a collocation method which directly obtain the numerical solution from the strong form. Therefore, we perform the integration by parts on (14) to obtain the Euler-Lagrange equation, i.e.,

$$\int_{\Omega} \left[ 2(d_{i} - 1)\mathcal{H}_{n}^{i} \delta d_{i} + \frac{G_{c}}{l_{0}} d_{i} \delta d_{i} - \nabla \cdot (G_{c} l_{0} \mathbf{A}_{i} \cdot \nabla d_{i}) \, \delta d_{i} + \beta_{p} (d_{i} - 1) \, \delta d_{i} \right] d\Omega 
+ \int_{\partial \Omega} G_{c} l_{0} \nabla d_{i} \cdot \mathbf{A}_{i} \cdot \mathbf{n} \delta d_{i} \, dS = 0,$$
(15)

where  $\partial \Omega$  is the boundary of the unit cell and  $\boldsymbol{n}$  is the unit normal. Note that the integration-by-part operation increases the continuity requirement of the cleavage energy  $G_c$ , the length scale  $l_0$ , the anisotropic tensor  $A_i$ , and the phase field  $d_i$ . Assuming that the cleavage energy  $G_c$ , the length scale  $l_0$ , and the anisotropic tensor  $A_i$  are periodic within the unit cell, then the surface integration term in Eq. (15) vanishes considering that the phase field gradient  $\nabla d_i$  is periodic while the surface normal  $\boldsymbol{n}$  is anti-periodic. The Euler-Lagrange equation of the multi-phase-field functional yields:

$$2(d_{i}-1)\mathcal{H}_{n}^{i} + \frac{G_{c}}{l_{0}}d_{i} - \nabla \cdot (G_{c}l_{0}\mathbf{A}_{i}) \cdot \nabla d_{i} - G_{c}l_{0}\mathbf{A}_{i} : (\nabla \nabla d_{i}) + \beta_{p}(d_{i}-1) = 0, \quad d_{i} \in \mathcal{H}_{\#}^{2}.$$
(16)

In practice, piece-wise constant cleavage energy  $G_c$ , length scale  $l_0$ , and anisotropic tensor  $A_i$  are mostly used, for example, in polycrystalline material or composite material. However, setting material parameters to be piecewise constant will introduce jump condition in Eq. (16), and therefore not feasible. This problem is circumvented in Eq. (17) by adopting the following approximations: (1) use  $\delta$  function at the grid points as the test function  $\delta d_i$ ; (2) assume the gradient of  $G_c$ ,  $l_0$ , and  $A_i$  are zero at all grid points. Then, the simplified Euler-Lagrange equation yields:

$$2(d_i - 1)\mathcal{H}_n^i + \frac{G_c}{l_0}d_i - G_c l_0 A_i : (\nabla \nabla d_i) + \beta_p (d_i - 1) = 0, \quad d_i \in H_\#^2,$$
(17)

where the phase field  $d_i$  lives in a high order smooth function space. The solution of the simplified strong form (17) is an approximation to the real solution which minimizes the total energy potential  $\Psi$ .

Remark 1. Remark on the length scale parameters in multi-phase-field models. In general, the length scale parameter of the phase field models equipped with a specific degradation function can be identified from experiments where a validation exercise that relates peak stress to material parameters, length scales (cf. Pham et al. [74], Choo and Sun [16]) after quantifying the amplification factor of the fracture energy due to spatial discretization (cf. [2]. In principle, this validation exercise could be extended to multi-phase-field and higher-order-phase field models. In the case of the higher-order-phase field models, it might be possible to identify the fracture energy as a function of orientation by having multiple experiments for the same specimen of different orientations. In the case of the multiphase-field models, the multiple phase field governing equations lead to great flexibility where a wide spectrum of fracture behaviors can be replicated by different combinations of degradation mechanism, driving force, length scale and anisotropy of fracture energy, as demonstrated in Quintanas-Corominas et al. [28], Blever and Alessi [30]. In this work, we assume that all the damage mechanisms for the multi-phase-field model employs the same form of degradation function, regularization term and length scale parameter. This treatment reduces the number of material parameters required for the models and therefore simplifies the inverse problems required to identify the material parameters. However, it is possible that there are situations in which enhancing the multi-phase-field models by enabling different length scale parameters, regularized profiles or forms of degradation functions can be beneficial for replicating more complex crack nucleation and propagation behaviors. While the calibration and validation of phase field fracture is an ongoing research topic that rightfully attracts considerable interest, the design of inverse problems, experimental procedure and the experiments themselves for the strongly anisotropic phase field models are out of the scope of these studies and will be considered in the future.

#### 2.2.2. Spatial discretization and numerical solution

The coupled mechanical and phase field equations can be solved in a staggered fashion. In this work, the mechanical step that solves the balance of linear momentum (13) is incrementally updated via the Fourier–Galerkin method [47,75]. The FFT-based solution method of the anisotropic phase field evolution equation (17) is presented in detail in this paper.

The phase field evolution equation (17) is a linear equation with respect to the i th phase field. These equations are solved in a semi-implicit way, where the phase field  $(d_j, j \neq i)$  of the last iteration is used to calculate the partial damaged strain energy  $\mathcal{H}_n^i$ . Then, the strong form (17) can be re-formulated by calculating the second order gradient in the Fourier space, which leads to the discretized form:

$$\left(2\mathcal{H}_n^i + \frac{G_c}{l_0} + G_c l_0 \mathbf{A}_i : \mathcal{F}^{-1} \boldsymbol{\xi} \otimes \boldsymbol{\xi} \mathcal{F} + \beta_p\right) d_i = 2\mathcal{H}_n^i + \beta_p. \tag{18}$$

Since the stiffness matrix is generally non-symmetric, this equation can be solved relatively efficiently by a matrix-free iterative linear solver, for example biconjugate gradient method (BiCG) or generalized minimal residual method (GMRES).

Note that in the discretized form (17), second order gradient is involved. Therefore, the solution of the discrete equation (17) suffers from the Gibbs effect when the continuum frequency vector is used, especially at the boundary of the fully damaged region and the partially damaged region where the first order gradient is discrete. The discrete frequency vector from Willot et al. [62] is generalized to higher order gradient case in order to overcome this problem. The backward finite difference scheme is used to calculate the discrete frequency vector  $k_i$ 

$$\mathbf{k} = \exp(i\mathbf{\xi}) - 1,\tag{19}$$

where i is the complex number unit and  $\xi$  is the continuum frequency vector defined as

$$\xi_i = \frac{2\pi n_i}{N}, \quad n_i = \begin{cases} -N/2, \dots, N/2 + 1 &, \mod(N, 2) = 0\\ -(N-1)/2, \dots, (N-1)/2 &, \mod(N, 2) = 1 \end{cases}$$
(20)

Here, N is the total number of grid points. The discrete frequency vector (19) is generalized to enable second order gradient based on the central difference rule, which in the 2D case reads:

$$\begin{cases} k_{xx} = 2(\cos \xi_x - 1) \\ k_{yy} = 2(\cos \xi_y - 1) \\ k_{xy} = -\sin \xi_x \sin \xi_y \end{cases}$$
 (21)

The second order gradient of a scalar field  $\phi$  can be calculated as  $\phi_{xx} = \mathcal{F}^{-1}[k_{xx}\hat{\phi}], \ \phi_{yy} = \mathcal{F}^{-1}[k_{yy}\hat{\phi}],$  and  $\phi_{xy} = \mathcal{F}^{-1}[k_{xy}\hat{\phi}],$  where  $\hat{\phi}$  denotes the Fourier coefficient of  $\phi$ . The second order discrete frequency vector (21) can be easily generalized to 3D case.

# 2.3. High-order phase-field model

In high-order phase-field theory, the total potential  $\Psi$  is split into the strain potential and the cleavage energy potential in the same way as (1). Instead of using multiple phase field for each preferential crack propagation direction, the crack density contains a high-order phase field gradient term to construct a non-convex functional. In this section, the fourth order phase-field theory is first re-derived in a periodic unit cell together with corresponding Euler-Lagrange equation. Then details are presented to solve the coupled mechanical and high-order phase-field in a staggered way using FFT-based method.

# 2.3.1. Phase field theory in periodic unit cell

In the high-order phase-field fracture theory, crack density function depends on the phase field as well as the first and second gradients of the phase field itself, i.e.,

$$\gamma(d, \nabla d, \nabla \nabla d) = \frac{1}{2l_0} d^2 + \frac{l_0}{4} \nabla d \cdot \nabla d + \frac{l_0^3}{32} (\nabla \nabla d) : \mathbb{A} : (\nabla \nabla d) + \frac{1}{2} \beta_p (d - 1)^2, \quad d \in H^2_{\#}(\Omega). \tag{22}$$

Again,  $H_{\#}^2(\Omega)$  denotes the space of periodic functions with square integrable second order gradient,  $\mathbb{A}$  is a fourth order anisotropic tensor to accommodate more complex anisotropies, and the numerical parameter  $\beta_p \gg 1$  serves to enforce the initial phase field. The structural tensor  $\mathbb{A}$  is invariant with respect to rotations from the cubic group. For materials belongs to cubic symmetry group, for example rock salt, the fourth order anisotropic tensor can be defined as

$$\mathbb{A} = \mathbb{I} + \alpha_{ha}(A_1 \otimes A_1 + A_2 \otimes A_2) + \beta_{ha} \operatorname{sym}(A_1 \otimes A_2), \tag{23}$$

where  $\mathbb{I}$  is the fourth order symmetric identity tensor,  $\alpha_{ha}$  and  $\beta_{ha}$  are two penalty parameters, and  $A_1$  and  $A_2$  are two second order structural tensors which are also invariant with respect to rotations from the cubic symmetry group. These second order tensors  $A_1$  and  $A_2$  are defined as

$$A_1 = a_1 \otimes a_1, \quad A_2 = a_2 \otimes a_2, \tag{24}$$

where the unit vectors  $\{a_i\}_{i=1,2,3}$  represents an orthonormal basis, which are related to the material point orientation and satisfy  $a_i \cdot a_j = \delta_{ij}$ ,  $a_i \times a_j = \epsilon_{ijk}a_k$ . The isotropic high-order phase-field theory can be recovered by setting  $\alpha_{ha} = \beta_{ha} = 0$ .

Then, the total crack surface area is the integral of the crack surface density over the periodic unit cell  $\Omega$ :

$$\Gamma_l(d) = \int_{\Omega} \gamma (d, \nabla d, \nabla \nabla d) \, \mathrm{d}\Omega. \tag{25}$$

Substitute this expression into the total potential (1) and take first order variation to minimize the total potential  $\Psi$  defined in Eq. (1).

In order to find the phase field d which minimizes the total potential  $\Psi$  defined in Eq. (1), the stationary condition is reached by taking first order variation over d:

$$\int_{\Omega} \left[ 2(d-1)\mathcal{H}_{1}^{1}\delta d + G_{c} \left( \frac{1}{l_{0}}d\delta d + \frac{l_{0}}{2}\nabla d \cdot \nabla \delta d + \frac{l_{0}^{3}}{16}\nabla \nabla d : \mathbb{A} : \nabla \nabla \delta d + \beta_{p} (d-1)\delta d \right) \right] d\Omega 
= 0, \, \forall \delta d \in H_{\#}^{2},$$
(26)

where  $\delta d$  is arbitrary phase field perturbation from  $H_{\#}^2$  space. Note that the partial strain energy  $\mathcal{H}_1^1$  is defined in Eq. (6) with total number of phase fields n equal to 1. Then integration by parts is performed to get the Euler equation of this problem.

$$\int_{\Omega} \left[ 2 (d-1) \mathcal{H}_{1}^{1} + \frac{G_{c}}{l_{0}} d - \nabla \cdot \left( \frac{G_{c} l_{0}}{2} \nabla d \right) + \nabla \cdot \nabla \cdot \left( \frac{G_{c} l_{0}^{3}}{16} \mathbb{A} : \nabla \nabla d \right) + \beta_{p} (d-1) \right] \delta d d \Omega 
+ \int_{\partial \Omega} \left[ \frac{G_{c} l_{0}}{2} \nabla d \cdot \mathbf{n} + \frac{G_{c} l_{0}^{3}}{16} \nabla \nabla d : \mathbb{A} : (\nabla \delta d \otimes \mathbf{n}) - \frac{G_{c} l_{0}^{3}}{16} \nabla \cdot (\mathbb{A} : \nabla \nabla d) \cdot \mathbf{n} \delta d \right] dS = 0.$$
(27)

Note that, similar to Eq. (15), the surface integral term only vanishes when the anisotropic tensor  $\mathbb{A}$  and the cleavage energy density  $G_c$  are periodic, and the length scale  $l_0$  is constant. Then we get the following Euler equation which minimizes the total potential  $\Psi$ :

$$2(d-1)\mathcal{H}_{1}^{1} + \frac{G_{c}}{l_{0}}d - \nabla \cdot \left(\frac{G_{c}l_{0}}{2}\nabla d\right) + \nabla \cdot \nabla \cdot \left(\frac{G_{c}l_{0}^{3}}{16}\mathbb{A}:\nabla\nabla d\right) + \beta_{p}(d-1) = 0.$$

$$(28)$$

This strong form can be further simplified by assuming that  $G_c$  and  $\mathbb{A}$  are piecewise constant:

$$2(d-1)\mathcal{H}_{1}^{1} + \frac{G_{c}}{l_{0}}d - \frac{G_{c}l_{0}}{2}\nabla \cdot \nabla d + \frac{G_{c}l_{0}^{3}}{16}\mathbb{A} :: \nabla\nabla\nabla\nabla d + \beta_{p}(d-1) = 0, \quad d \in H_{\#}^{4}.$$
(29)

The reason for such simplification can be found in Section 2.2.1. This assumption is true for many material models, for example crystal plasticity, where the preferential cleavage direction is constant within the grain, while the transition between two adjacent grains is sharp. This assumption does not hold for functionally graded material where a smooth variation of the preferential crack propagation direction exists. This equation, when solved by finite element method in its weak form, requires  $C^1$  continuous shape functions. However, when this equation is solved by collocation method in its strong form, fourth order differentiable interpolation functions are required. The FFT-based method offers a way to solve this equation in its strong form, where the trigonometric polynomial shape functions are arbitrary order differentiable.

#### 2.3.2. Spatial discretization and numerical solution

The strong form (29) is a linear equation and can be re-formulated when the fourth order gradient is calculated in Fourier space:

$$\left(2\mathcal{H}_1^1 + \frac{G_c}{l_0} + \frac{G_c l_0}{2} \mathcal{F}^{-1} \boldsymbol{\xi} \cdot \boldsymbol{\xi} \mathcal{F} + \frac{G_c l_0^3}{16} \mathbb{A} :: \mathcal{F}^{-1} \boldsymbol{\xi} \otimes \boldsymbol{\xi} \otimes \boldsymbol{\xi} \otimes \boldsymbol{\xi} \mathcal{F} + \beta_p\right) d = 2\mathcal{H}_1^1 + \beta_p. \tag{30}$$

Note that different from multi-phase-field where the updated phase field  $d_i$  can only be solved semi-implicitly, the high-order phase-field equation can be solved fully implicitly since the partial strain energy  $\mathcal{H}_1^1$  is independent of phase field. Since the stiffness matrix is generally non-symmetric, this equation can be solved by matrix-free iterative linear solver, for example biconjugate gradient method (BiCG) or generalized minimal residual method (GMRES).

Similarly to the multi-phase-field, continuous frequency vector and discrete frequency vector are defined in (19) and (20), respectively. In order to calculate fourth order gradient without suffering from Gibbs effect, the following discrete frequency vector is suggested

$$\begin{cases} k_{xxxx} = 4(\cos \xi_x - 1)^2 \\ k_{xxxy} = -2\sin \xi_x \sin \xi_y (\cos \xi_x - 1) \\ k_{xxyy} = 4(\cos \xi_x - 1)(\cos \xi_y - 1) \\ k_{xxyy} = -2\sin \xi_x \sin \xi_y (\cos \xi_y - 1) \\ k_{yyyy} = 4(\cos \xi_y - 1)^2, \end{cases}$$
(31)

where  $\xi$  is the continuous frequency vector defined in (20). The fourth order gradient of a scalar field  $\phi$  can be calculated as  $\phi_{xxxx} = \mathcal{F}^{-1}[k_{xxxx}\hat{\phi}], \ \phi_{xxxy} = \mathcal{F}^{-1}[k_{xxxy}\hat{\phi}], \ \phi_{xxyy} = \mathcal{F}^{-1}[k_{xxyy}\hat{\phi}], \ \phi_{xyyy} = \mathcal{F}^{-1}[k_{xyyy}\hat{\phi}], \ \text{where } \hat{\phi} \text{ denotes the Fourier coefficient of } \phi$ . The fourth order discrete frequency vector (31) can be easily generalized to 3D case.

**Remark 2.** The iterative linear solver can be accelerated by a suitable preconditioner M. In this paper, a finite difference matrix is constructed based on the isotropic part of the linear equations (17) and (29). The Laplace operator is approximated by the five-point stencil with periodic boundaries. The incomplete Cholesky decomposition of this finite difference matrix is utilized as the preconditioner M. Also, the phase field of the previously converged step is used as the initial guess to further accelerate the linear solver.

#### 2.4. Regularized interface fracture model for grain boundaries

The macroscopic failure of materials with microstructures formed by assemblies of grains, layers, laminates, or other forms of building blocks can be triggered by a combination of intergranular fracture and intragranular fracture.

Examples of these materials include polycrystal, sedimentary rock, biological tissues, and composite materials [76]. As a result, a good combination of bulk and interfacial fracture models is essential to capture the essence of failures.

In the phase field fracture literature, there are different approaches to simulate the competition between intergranular fracture and intragranular fracture. One approach is to explicitly define an additional interface region in a discretized mesh. An interface crack propagation model with interface-normal based anisotropic tensor  $A = n \otimes n$  and reduced cleavage energy  $G_c$  is assigned to the interface region [27]. This treatment is relatively simple, as both the fracture inside the grain and along the grain boundaries can be captured by the same phase field. Another approach is to approximate the cohesive fracture displacement jump  $[\![u]\!]$  with a regularized auxiliary field v by utilizing the initial equilibrium grain boundary phase field, such that explicit mesh discretization for an additional interface region is avoided [26,29,77,78]. In this approach, the phase field model is used to model the crack growth inside the grain, while a cohesive zone model is used to replicate the complex crack behaviors of grain boundaries with richer descriptions enabled by the cohesive zone models [78].

For simplicity, we adopt the first approach is to represent the sharp interface via a regularized diffusive region associated with a characteristic length scale. As such, an interface region is explicitly identified via an implicit function and the spatial domain is partitioned after a realization of polycrystal structure is generated via a mesh generator. The major assumption is that the interface phase field fracture model is transverse isotropic with respect to the normal direction of an interface or grain boundary. For multi-phase-field, a simple approach is used by assigning one of the principal directions of the symmetric anisotropic tensor A parallel to the interface normal for the governing equations of all the phase field variables. For high-order phase-field, a fourth order anisotropic tensor A invariant to the rotation from transverse isotropy group is utilized (cf. Li and Maurini [79]):

$$\begin{bmatrix} C_{11} & C_{11} - 2C_{66} & C_{13} & 0 & 0 & 0 \\ C_{11} - 2C_{66} & C_{11} & C_{13} & 0 & 0 & 0 \\ C_{13} & C_{13} & C_{33} & 0 & 0 & 0 \\ 0 & 0 & 0 & C_{44} & 0 & 0 \\ 0 & 0 & 0 & 0 & C_{44} & 0 \\ 0 & 0 & 0 & 0 & 0 & C_{66} \end{bmatrix}.$$

$$(32)$$

In order for the 4th order stiffness tensor (32) to be positive definite, the following conditions have to be met [80]:

$$2C_{13}^2 < C_{33} (C_{11} + C_{12}), C_{44} > 0, C_{66} > 0. (33)$$

Triple junctions and quadruple points are assumed to be isotropic with 4th order identity tensor.

# 2.5. Discrete algorithm

The coupled mechanical and phase field equations are solved in a sequential manner, and the algorithm is shown in Algorithm 1. Within each step, the mechanical problem is first solved with the help of the Green's operator  $\mathbb{G}$ . The essential boundary conditions and natural boundary conditions are satisfied in two coupled Newton–Raphson iterations. Detailed theory and implementation of the mechanical part can be found in Zeman et al. [75], Ma and Truster [47]. After the mechanical problem converges within the required tolerance, the linear phase field equations are then solved by an iterative linear solver, for example conjugate gradient or generalized minimal residual method (GMRES). Although the two governing equations are solved sequentially, it has been shown that the final solution could converge to the exact solution when the time step is smaller than the critical time step, a important feature shared by phase field equations solved via finite element methods e.g. Wheeler et al. [81], Miehe et al. [82], Ambati et al. [83], Wang and Sun [5], Bryant and Sun [9].

#### 3. Analysis and numerical examples

In this section, we compare the accuracy and efficiency of the FFT-based solvers for multi-phase-field and high-order phase-field. First, the one-dimensional equilibrium phase field with central concentrated failure is solved using the FFT-based method for both the low-order and high-order phase field. Special attention is paid to compare the Gibbs effect manifested in both models, as well as the convergence rate and performance. Then, a two-dimensional benchmark case is used to demonstrate and benchmark the ability of the FFT-based method in solving strongly anisotropic fracture problems, more specifically the sawtooth crack pattern observed in strongly anisotropic fracture.

# Algorithm 1: FFT-based algorithm for strongly anisotropic phase field problem.

```
1 for n \leftarrow 1 to ustep do
                     if Strain boundary condition then \Delta \bar{\boldsymbol{\varepsilon}} = \Delta \bar{\boldsymbol{\varepsilon}}_{BC}
  2
                     else \Delta \bar{\boldsymbol{\varepsilon}} = \bar{\boldsymbol{C}}_n^{-1} \Delta \bar{\boldsymbol{\sigma}}_{BC}
  3
  4
                                \boldsymbol{\varepsilon}_{n+1} = \boldsymbol{\varepsilon}_{n+1} + \Delta \bar{\boldsymbol{\varepsilon}}
  5
                                solve for \Delta \tilde{\boldsymbol{\varepsilon}} : \mathbb{G} * (\boldsymbol{C}_n : \Delta \tilde{\boldsymbol{\varepsilon}}) = -\mathbb{G} * (\boldsymbol{C}_n : \Delta \bar{\boldsymbol{\varepsilon}})
  6
                                update \boldsymbol{\varepsilon}_{n+1}: \boldsymbol{\varepsilon}_{n+1} = \boldsymbol{\varepsilon}_{n+1} + \Delta \tilde{\boldsymbol{\varepsilon}}
  7
                                while R > \text{tol. do}
  8
                                           update \sigma_{n+1}: \sigma_{n+1} = f(\Delta \varepsilon, \sigma_n, \text{history})
                                           solve for \Delta \tilde{\boldsymbol{\varepsilon}}: \mathbb{G} * (\boldsymbol{C}_{n+1} : \Delta \tilde{\boldsymbol{\varepsilon}}) = -\mathbb{G} * \boldsymbol{\sigma}_{n+1}
10
                                           update \boldsymbol{\varepsilon}_{n+1}: \boldsymbol{\varepsilon}_{n+1} = \boldsymbol{\varepsilon}_{n+1} + \Delta \tilde{\boldsymbol{\varepsilon}}
11
                                           update residual: R = \|\Delta \tilde{\boldsymbol{\epsilon}}\|
12
                                end
13
                                \bar{\boldsymbol{\sigma}} = \langle \boldsymbol{\sigma}_{n+1} \rangle
14
                               if \frac{\|\bar{\sigma} - \sigma_{BC}\|}{\|\bar{\sigma}\|} < \text{tol. then break}
                                update \bar{C}_{n+1}
16
                               update \Delta \bar{\boldsymbol{\varepsilon}} : \Delta \bar{\boldsymbol{\varepsilon}} = -\bar{\boldsymbol{C}}_{n+1}^{-1} (\bar{\boldsymbol{\sigma}} - \boldsymbol{\sigma}_{BC})
17
18
                     Update phase field
19
                    if Multi-phase-field then
20
                                \left(2\mathcal{H}_n^i + \frac{G_c}{l_0} + G_c l_0 \mathbf{A}_i : \mathcal{F}^{-1} \boldsymbol{\xi} \otimes \boldsymbol{\xi} \mathcal{F} + \beta_p\right) d_i = 2\mathcal{H}_n^i + \beta_p.
21
                    else if High-order phase-field then
22
                                 \left(2\mathcal{H}_{1}^{1} + \frac{G_{c}}{l_{0}} + \frac{G_{c}l_{0}}{2}\mathcal{F}^{-1}\boldsymbol{\xi} \cdot \boldsymbol{\xi}\mathcal{F} + \frac{G_{c}l_{0}^{3}}{16}\mathbb{A} :: \mathcal{F}^{-1}\boldsymbol{\xi} \otimes \boldsymbol{\xi} \otimes \boldsymbol{\xi} \otimes \boldsymbol{\xi}\mathcal{F} + \beta_{p}\right)d = 2\mathcal{H}_{1}^{1} + \beta_{p}
23
24 end
```

Again, the convergence progress of the multi-phase field and high-order phase-field is compared. Finally, a three-dimensional polycrystalline rock salt example is presented to illustrate the competing between intergranular and intragranular fracture in polycrystals.

#### 3.1. One-dimension verification and convergence analysis

An one-dimensional phase-field distribution problem from Borden et al. [14] is used as an example to assess the accuracy of the FFT solver as well as examine the numerical solutions obtained via the FFT-based method in solving phase field problems in periodic domains. Consider a rod with a concentrated flaw in the middle. This concentrated flaw can be represented by prescribing the phase field value at this point to be 1. The governing equation of the phase field model then yields the initial phase field distribution. Without applying any external loading, there exists an exact solution that governs the phase field distribution in the one-dimensional setting. The multi-phase-field governing equation and the corresponding analytical solution reads,

$$d - 4l_0^2 d'' + \beta_p d = \beta_p, \quad d(x) = \exp\left(\frac{-|x|}{2l_0}\right). \tag{34}$$

Meanwhile, the high-order phase-field governing equation together with its analytical solution reads,

$$d - 2l_0^2 d'' + l_0^4 d^{(4)} + \beta_p d = \beta_p, \quad d(x) = \left(1 + \frac{|x|}{l_0}\right) \exp\left(\frac{-|x|}{l_0}\right). \tag{35}$$

In our numerical example, the length of the rod is 200 to be consistent with the results in Borden et al. [14]. The initial phase field penalty  $\beta_p$  is 1000 at x=0 and 0 elsewhere. The length scale parameter  $l_0$  is 0.08.

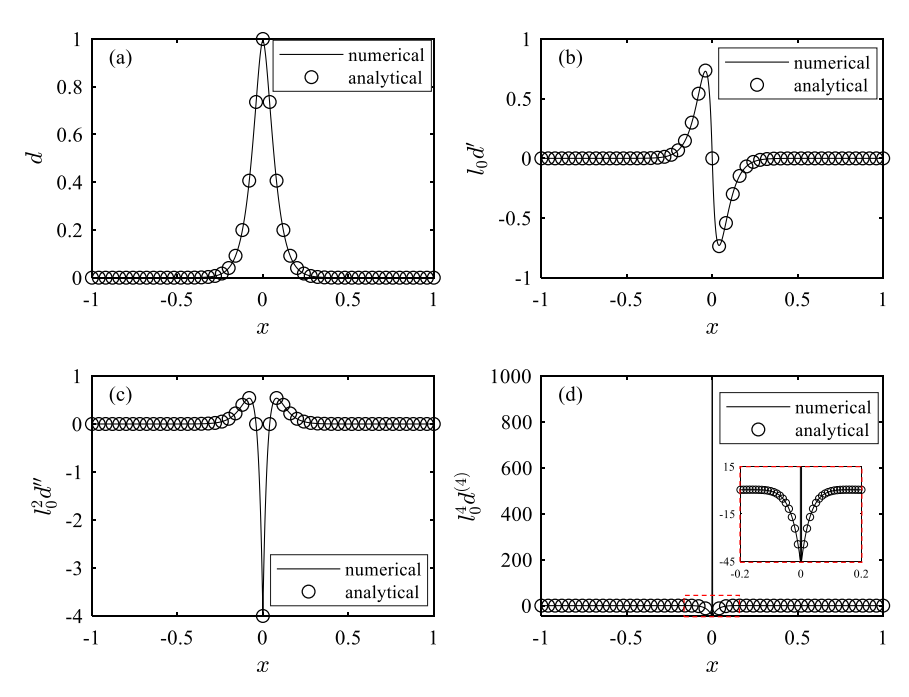


Fig. 3. Verification of 1D phase field distribution against analytical solution. The second order derivative is required by multi-phase-field, while the fourth order derivative is required by high-order phase field. (a) Phase field (d(x)); (b) First derivative  $(l_0d'(x))$ ; (c) Second derivative  $(l_0^2d''(x))$ ; (d) Fourth derivative  $(l_0^4d^{(4)}(x))$ .

These phase-field partial differential equations are solved numerically in FFT-based method (17) and (29). The numerical solution is then integrated over the rod to get the numerical potential  $\Psi$  based on (1). The surface energy potential that leads to the exact solution of the phase field distribution in (34) and (35) reads,

$$\Psi_c = 2G_c \int_0^{100} \left[ \frac{d^2}{4l_0} + l_0(d')^2 \right] dx \approx G_c, \tag{36}$$

for multi-phase-field, and the surface energy potential for the exaction solution for the high order phase field problem reads,

$$\Psi_c = 2G_c \int_0^{100} \left[ \frac{d^2}{4l_0} + \frac{l_0}{2} (d')^2 + \frac{l_0^3}{4} (d'')^2 \right] dx \approx G_c, \tag{37}$$

which again corresponds with the high-order phase-field solution in Borden et al. [14].

Fig. 3 compares the numerical and analytical solutions, the corresponding first order derivatives  $(l_0^d d')$ , the second order derivatives  $(l_0^2 d'')$ , as well as the fourth order derivatives  $(l_0^4 d^{(4)})$ . Both the phase field and its high-order derivative fits with the analytical solutions, except at the position x = 0 where the fourth order derivative of the analytical solution is supposed to be undefined whereas the numerical solution remains finite due to the differentiability of the sine and cosine functions.

The Gibbs phenomenon is not observed even for the fourth order derivative near the initial failure point where large phase field gradient exists. These results suggest that the backward discrete frequency scheme [62] combined with the generalized discrete frequency vector for high-order gradient (21) and (31) is effective in eliminating the Gibbs phenomenon that might otherwise cause spurious oscillations. It needs to be mentioned that the solution based on continuous frequency vector suffers from the Gibbs phenomenon, while the solution based on other discrete frequency vector schemes, for example the forward scheme and the central scheme from Willot et al. [62], does not converge to the analytical solution upon refinement. Corresponding results are not presented for brevity.

The error in the surface energy potential,  $G^{num} - G_c$ , is presented in Fig. 4(a). Under the same mesh refinement, the high-order phase-field has lower surface energy error than multi-phase-field. The h-convergence rate is about 0.72 for multi-phase-field, while 1.01 for high-order phase-field. The faster convergence rate of the high-order

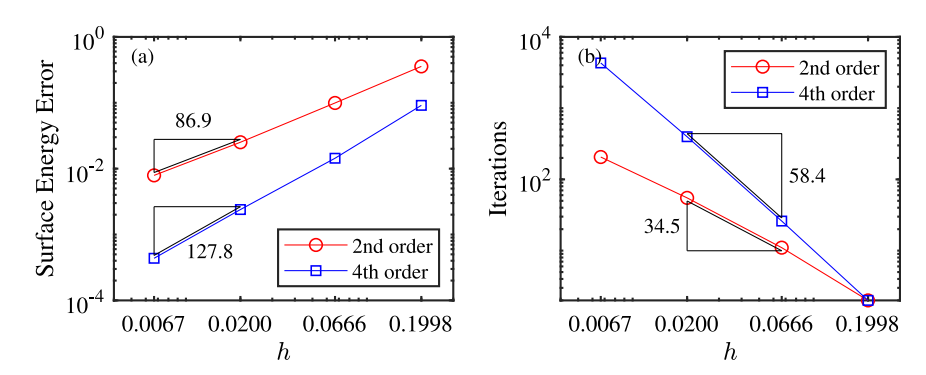


Fig. 4. Convergence behavior of phase field under no external loading: (a) Convergence plot upon mesh refinement; (b) Convergence progress of iterative linear solver (without preconditioning).

| Table 1  |            |    |     |           |     |     |           |              |
|----------|------------|----|-----|-----------|-----|-----|-----------|--------------|
| Material | properties | of | the | specimens | for | the | numerical | simulations. |
|          |            | _  |     |           |     |     |           |              |

| Parameters    | Description                                  | Value                | Unit                        |
|---------------|--|----------------------|-----------------------------|
| E             | Elastic modulus                              | 38.0                 | GPa                         |
| ν             | Poisson's ratio                              | 0.25                 | _                           |
| $\beta_p$     | Initial phase field penalty                  | 1000.0               | -                           |
| $\hat{G_c}$   | Cleavage energy                              | 1.15                 | $\mathrm{J}\mathrm{m}^{-2}$ |
| $l_0$         | Length scale                                 | $1.0 \times 10^{-5}$ | m                           |
| $\beta_{ma}$  | Anisotropy factor for multi-phase-field      | 40.0                 | -                           |
| $\alpha_{ha}$ | Anisotropy factor for high-order phase-field | 1.2                  | -                           |
| $\beta_{ha}$  | Anisotropy factor for high-order phase-field | 1000.0               | -                           |

phase-field upon mesh refinement is at the expense of the lower linear solver convergence rate. The linear solver convergence rate of the strong form (17) and (29) is presented in Fig. 4(b). The convergence efficiency of both models becomes lower upon each mesh refinement, indicating that the condition number of the stiffness matrix becomes larger each upon mesh refinement. Furthermore, our numerical experiment indicates that the high-order phase-field requires significantly more iterations (more than one order) to converge than the low-order phase-field counterpart. Note that, in the multi-dimensional cases, the number of independent phase field required to replicate anisotropy of the surface energy likely increases according to the complexity of the anisotropic responses. Hence, the 2nd-order phase field governing equation must be solved multiple times, while there is only one 4th-order phase field governing equation required for the higher-order case. This trade-off is further analyzed in the next two numerical examples.

#### 3.2. Two-dimensional plane strain single-crystal rock salt

A plane strain single crystal rock salt is used to demonstrate the numerical behavior of the FFT-based method in solving 2D phase field crack propagation problems. The room temperature elastic constants and phase field parameters are listed in Table 1 [7]. Although single crystal rock salt belongs to cubic symmetry group, the elastic anisotropic factor is almost 1, therefore isotropic elasticity model (3) is used here. The cleavage plane of single crystal rock salt is  $\{100\}$  plane. In order for the two-dimensional simulation to be able to represent the crack propagation, the [001] axis is set to coincide with the z axis while the single crystal deforms in the x-y plane.

In this section, a single crystal rock salt with a central concentrated flaw is first utilized to demonstrate the initial equilibrium phase field pattern and the convergence behavior of multi-phase-field and high-order phase-field. Then plane-strain tension test is presented to show the ability of both methods to represent the sawtooth crack pattern.

#### 3.2.1. Influence of frequency vector on numerical accuracy and stability

A two-dimensional plate with a central concentrated flaw is utilized to compare the numerical behavior of multiphase-field and high-order phase-field. The initial equilibrium phase field of both methods is solved using BiCG solver, with the relative tolerance  $1.0 \times 10^{-8}$ .

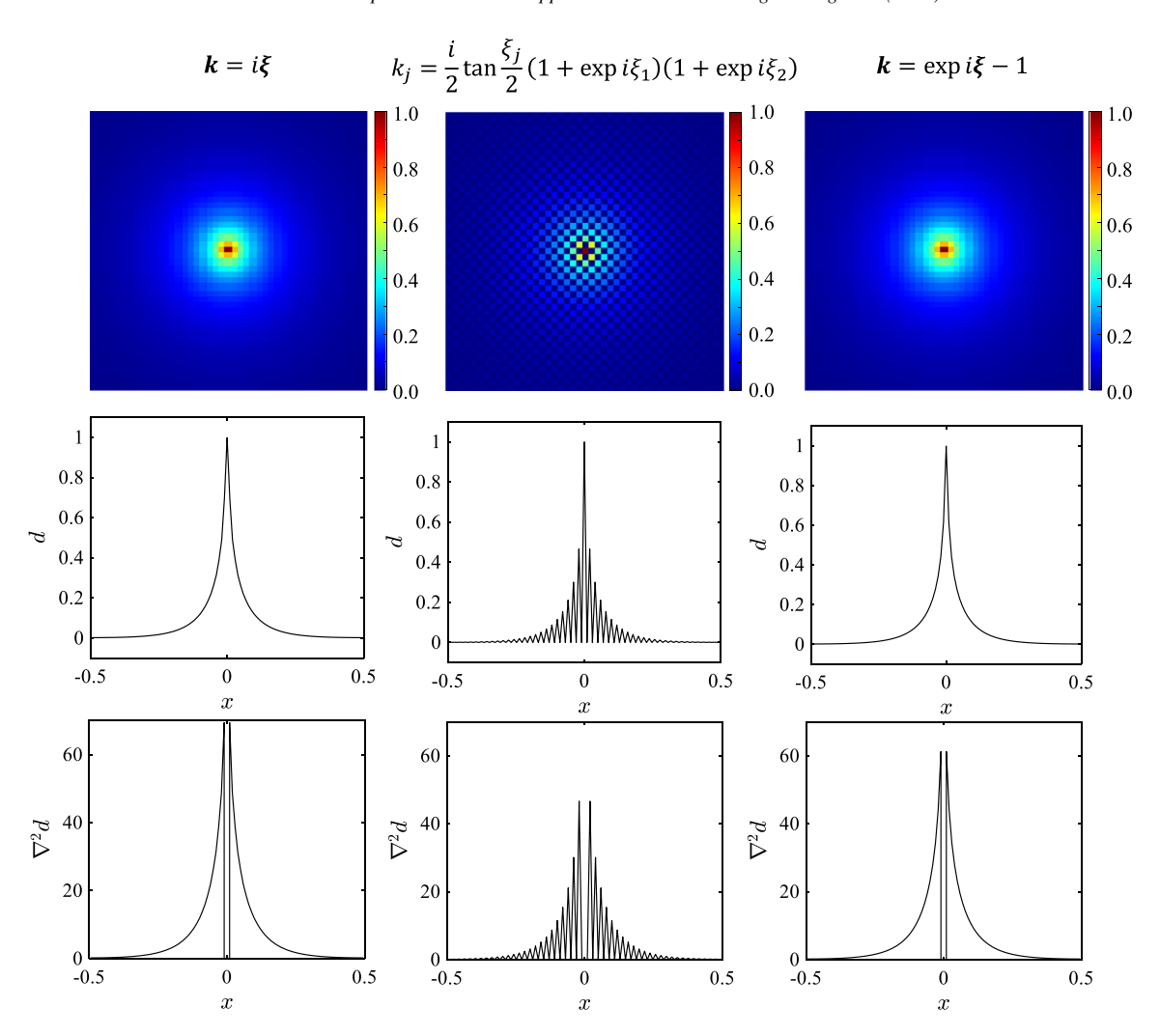


Fig. 5. Influence of discrete frequency vector on the accuracy and stability of the initial phase field distribution. Top: 2D phase field distribution; Middle: phase field distribution along the central line; Bottom: Laplacian of phase field. The anisotropic factor  $\beta_{ma}$  equal to zero for all three cases.

Fig. 5 compares the continuum frequency vector (left), rotated discrete frequency vector (middle), and forward-backward discrete frequency vector (right), regarding the accuracy and stability of the solution field. In all three cases, the initial equilibrium phase field is solved with the anisotropic factor  $\beta_{ma}=0$ . When the continuum frequency vector ( $\mathbf{k}=i\xi$  is used in Eq. (18), the phase field d and its Laplacian appears to be smooth without spurious oscillation. Actually, when a smaller length scale parameter  $l_0$  is used or high-order gradient is involved in the governing equation, the usage of continuum frequency vector often suffers from spurious oscillation. When the rotated scheme is used [58,59], numerical instability is observed in the solution, which is also reported elsewhere [58]. The instability is caused by the construction of the discrete frequency vector instead of the Gibbs phenomenon. When the rotated scheme is adopted, the real solution is metastable, while the solution shown in Fig. 5 appears to be more stable. This instability is easy to understand when centered scheme  $\mathbf{k}=i\sin\xi$  is used, where the instability is also observed, but less obvious for the rotated scheme. This also explains why the instability is less obvious as phase field propagates as reported [58]. Note that such instability is specific for this type of governing equation (17) and Eq. (29) where the unknown field and its Laplacian co-exist in one equation. This instability can be overcome by using the backward scheme (19) such that the unknown field and its gradient are smooth even when lower length scale  $l_0$  and higher order gradient is used, as already presented in Fig. 3.

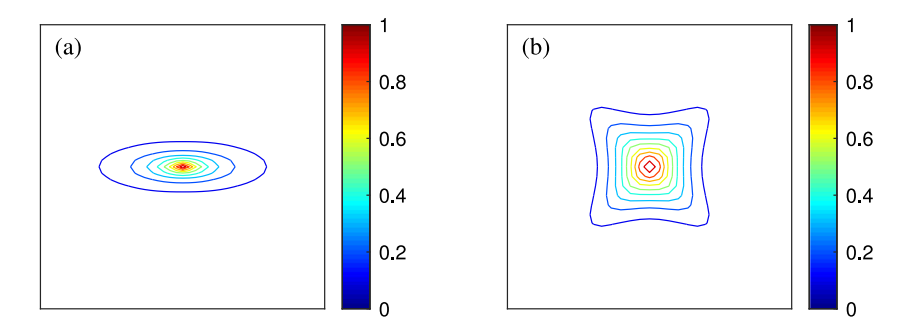


Fig. 6. Initial equilibrium phase field distribution with central point flaw: (a) Multi-phase-field method; (b) High-order phase-field method.

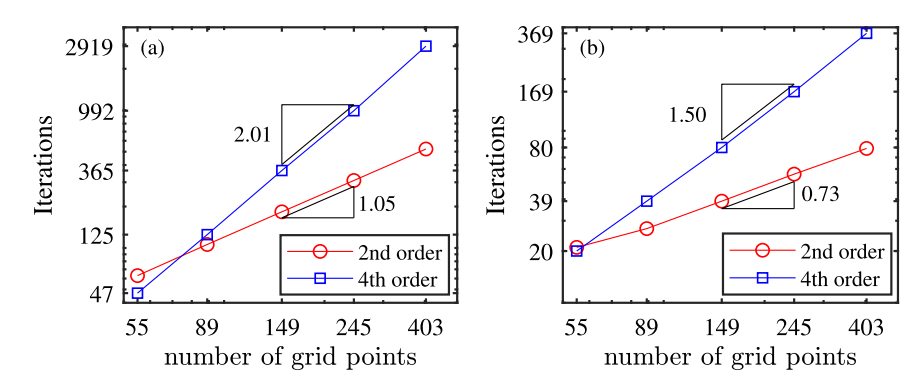


Fig. 7. Convergence rate of strongly anisotropic phase field upon mesh refinement: (a) Without preconditioning; (b) With preconditioning. Only one phase field variable is considered in multi-phase-field. Both multi-phase-field and high-order phase-field are solved by conjugate gradient. Note that the anisotropic factor (tensor) also influences the convergence behavior.

Fig. 6(a) and (b) shows the initial phase field distribution of multi-phase-field and high-order phase-field, respectively. For the multi-phase-field result, only one of the two phase field variables is shown. The high-order phase-field can represent the non-convex phase-field distribution observed in strongly anisotropic crack propagation. More importantly, the phase field distribution is smooth over the domain without local perturbation or Gibbs phenomenon observed.

Fig. 7(a) shows the convergence rate of the iterative linear solver for multi-phase-field (17) and high-order phase-field (29) without preconditioning. For lower mesh resolution, the computational costs of both methods are comparable, while for higher mesh resolution, high-order phase-field is more expensive. Note that only one linear equation is solved for high-order phase-field, while for multi-phase-field the number of linear equations depends on the total number of independent phase fields. Evidence gathered from the numerical examples suggested that, for lower mesh resolution, high-order phase-field is more efficient, while for higher mesh resolution, multi-phase-field is more efficient. Fig. 7(b) shows the corresponding convergence rate with preconditioning. The convergence rate of both multi-phase-field and high-order phase-field can be accelerated by using the aforementioned preconditioner in Remark 2. Nevertheless, the convergence rates still deteriorate with an increasing number of grid points, indicating that the condition number increases with more refined discretization. Without proper remedies, such as a suitable preconditioner, this attribute may limit the applications of the current FFT-based scheme to solve phase field equations in fine grids that lead to sizable large linear systems, for example image-based simulations. A comprehensive study on the remedy for this issue will be explored in a future study but is out of the scope of the research covered in this article.

## 3.2.2. Sawtooth crack pattern in single crystal rock salt

A two-dimensional single crystal rock salt simulation to illustrate the capability of both methods to reproduce sawtooth crack pattern which is typically observed in strongly anisotropic phase field models [31]. Fig. 8 shows the geometrical setup. A 3 mm by 1 mm single crystal rock salt is discretized into  $303 \times 101$  equally distributed grid

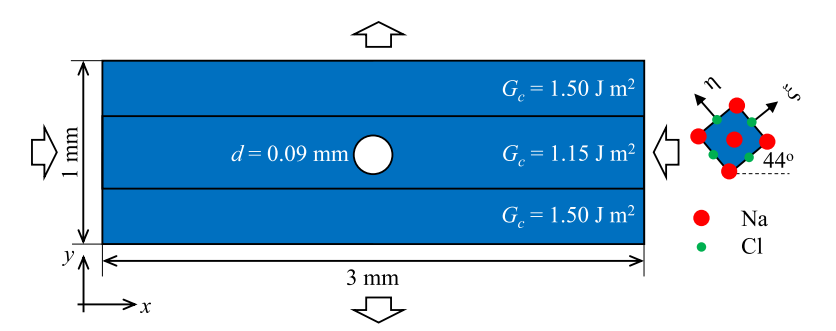


Fig. 8. Simulation setup of a two dimensional single crystal tension test with increased cleavage energy  $G_c$  in the top and bottom region. The diameter of the initial flaw is 0.09 mm. The NaCl crystal structure denotes the initial orientation of the single crystal sample.

points, so that the grid spacing is about 0.01 mm which is comparable to the length scale parameter  $l_0$ . A 0.09 mm diameter central hole is assigned unit initial phase field and serves as the crack nucleation site. The initial orientation of the single crystal rock salt is  $(44^{\circ}, 0^{\circ}, 0^{\circ})$  in Bunge Euler angle convention, such that one cleavage plane is  $(44^{\circ}$  to the loading direction while the other is  $(46^{\circ}$  to the loading direction. Two phase fields with perpendicular crack propagation direction are utilized in multi-phase-field, and a cubic symmetry fourth order structural tensor is used in high-order phase-field. The cleavage energy of the clamping region (top and bottom parts in Fig. 8) is slightly increased such that the crack will not penetrate through the boundary. The coupled mechanical and phase field equations are solved in a staggered manner, therefore a small strain increment is required to get convergent solution. Average strain boundary condition is prescribed:

$$\bar{\varepsilon} = \begin{bmatrix} -3.75 \times 10^{-4} & 0.0\\ 0.0 & 1.5 \times 10^{-3} \end{bmatrix}. \tag{38}$$

The total strain is equally divided into 1000 steps.

The sawtooth crack pattern, observed experimentally in Yuse and Sano [84], Takei et al. [85], is replicated in the current simulations for both the multi-phase-field case (Fig. 9(a)) and rgw high-order phase-field case (Fig. 9(b)).

Recall that the preferential cleavage plane of single crystal rock salt is  $\{001\}$ , and the initial orientation of the single crystal sample is shown in Fig. 8. Therefore, the two preferential cleavage planes in the plane strain tension simulation are oriented at 44° counter-clockwise and 46° clockwise from the horizontal direction. Upon loading, the crack initiates at the central hole where stress concentration exists, and propagates along the 46° energetically preferred direction. After the crack reaching the clamping region, the higher cleavage energy  $G_c$  of the material in the clamping region make propagating through the material a less energetic favorable configuration thank kinking with a different direction. Hence a kink is formed to allow the crack propagating along the second preferred direction (44° counter-clockwise from the horizontal direction). However, since the second preferred direction is not the most energetically preferred one once the crack tip is not crossing the tougher layer, the crack therefore kinks back to the first preferred direction before it reaches the clamping region. This process keeps repeating until the crack propagates through the specimen. In total, 6 kinks are observed in the multi-phase-field case, and 8 kinks are observed in the high-order phase-field case. In both cases, the crack kinks as it reaches the clamping boundary the first time while propagating along the first preferential direction. It then kinks before reaching the clamping boundary when propagating along the second preferential direction.

However, one key difference in the crack pattern is that the crack propagates less along the second preferential direction in high-order phase-field case than in the multi-phase-field case. Such a difference may be attributed to the different phase field anisotropy parameters as well as the periodic boundaries which may lead to different crack patterns than the non-periodic counterparts as reported in [7,79,86]. More details about the relations among preferred crack propagation direction, anisotropy of surface energy and the resultant kinking patterns on phase field simulations have been discussed in Li and Maurini [79], Li et al. [86] based on the quenching experiments reported in Yuse and Sano [84], Takei et al. [85].

In Fig. 9, the smearing damage region in the multi-phase-field model is wider than the high-order counterpart, although both models employ the same length scale parameter  $l_0$  to regularize the damage field. This difference

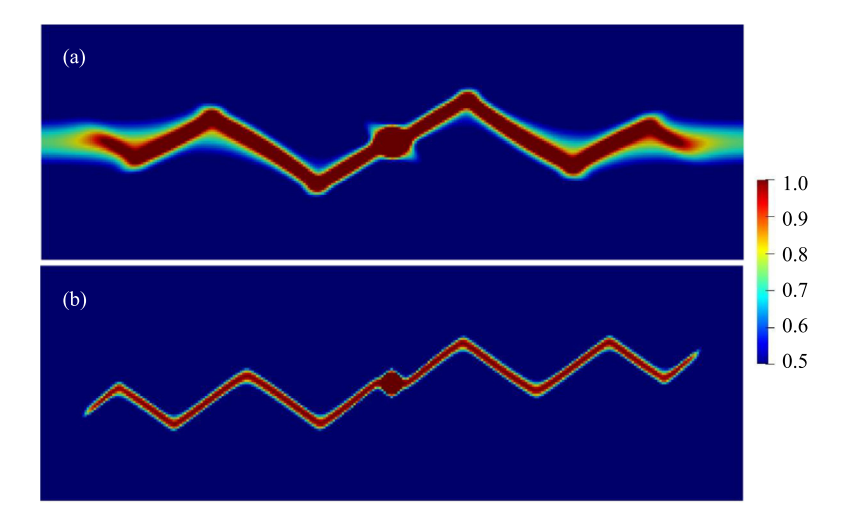


Fig. 9. Sawpath crack patterns simulated via the two strongly anisotropic phase field models (a) Multi-phase-field case; (b) High-order phase-field case.

can be attributed to the following factors. First, the multi-phase-field and high-order phase-field models are formulated via different energy functionals. The high-order phase-field has a more regularized spatial profile as the additional higher-order term of the governing equation controls the fourth-derivatives, while the lower-order governing equations of the multiple-phase-field model do not regulate the third- and fourth-derivative. The difference in profile shapes of the two models leads to different amounts of energy dissipated even if the driving force is identical [87]. Furthermore, since the multi-phase field model contains multiple phase field evolving around multiple driving forces, the phase field corresponding for different mechanisms may nucleate at different time and grow differently. Meanwhile, the damaged region of the higher-order phase field model is driven by only one phase field with one driving force. As a result, the difference in the results is expected.

# 3.3. Three-dimensional polycrystaline microstructure

In the third example, a multi-axial tension test performed on a three-dimensional polycrystalline rock salt specimen is simulated to examine the ability of the FFT-based method in solving strongly anisotropic crack propagation in polycrystals. The initial microstructure of the polycrystalline RVE is shown in Fig. 10, which is generated using the open source software Neper [88]. The  $1.0 \times 1.0 \times 1.0$  mm domain is equally discretized into 99<sup>3</sup> grid points, containing 40 equiaxed grains with random initial orientation. Therefore, the grid point spacing is about 0.01 mm which is comparable to the length scale parameter  $l_0$ . The material parameters are the same as the two-dimensional example and are listed in Table 1. For multi-phase-field method, three independent phase field variables are required to represent three {100} cleavage plane, and the preferential propagation direction is determined by the initial orientation of the grain. The grain boundary region with 0.03 mm thickness is explicitly meshed. All three phase field variables share the same crack propagation direction determined by the grain boundary normal for multi-phase-field, while transverse-isotropic structural tensor A is assigned to the grain boundary region for high-order phase-field. Again, triple junctions and quadruple points are assumed to be isotropic for simplicity and are assigned with identity structural tensor. A spherical void of diameter 0.06 mm is assigned with a prescribed phase field equal to unity and serves as the nucleation site. This initial flaw can be considered as the porous flaw typically exists at rock salt grain boundary. The coupled mechanical and phase field equations are solved in a staggered manner. Therefore, the strain increment has to be small for the solution to converge. A homogenized strain boundary condition is imposed onto the polycrystalline RVE.

$$\bar{\boldsymbol{\varepsilon}} = \begin{bmatrix} -3.75 \times 10^{-4} & 0.0 & 0.0 \\ 0.0 & 1.5 \times 10^{-3} & 0.0 \\ 0.0 & 0.0 & 0.0 \end{bmatrix}. \tag{39}$$

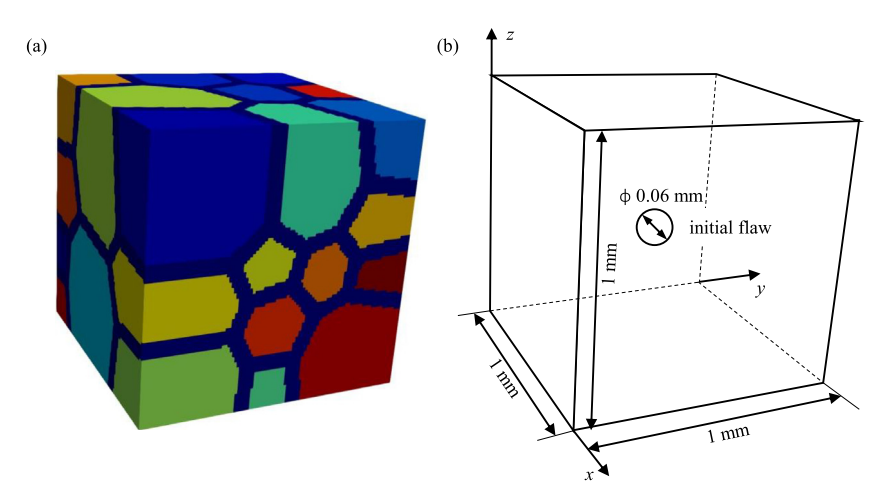


Fig. 10. Initial polycrystalline microstructure and simulation setup: (a) Polycrystalline RVE with finite thickness grain boundary region; (b) The spatial dimension of the RVE with a spherical flaw of 0.06 mm-diameter at the centroid of the RVE.

This total strain of the RVE is equally divided into 1000 incremental steps for numerical simulations.

The simulated three-dimensional strongly anisotropic crack propagation obtained from both models is shown in Fig. 11. While the multi-phase-field and high-order phase-field models do not yield the same crack pattern, both of them exhibit the influence of strongly anisotropic tensor A and  $\mathbb{A}$  on the crack pattern. The difference in crack patterns may be attributed to different types of regularization (2nd-order vs. 4th-order) used in both models, as well as the different ways damage is accumulated in the single- and multi-phase-field models. Nevertheless, since the grain boundary fracture remains the dominated damage mechanism in the RVE, the results of this simulation are likely to be even more sensitive to the choice of model used to replicate the grain boundary fracture [89] than the choice of the phase field fracture models for the bulk volume.

Furthermore, the anisotropic tensor penalizing the preferential crack direction, the reduced grain boundary cleavage energy may also influence the crack propagation pattern, as shown in Fig. 12. The grain boundary cleavage energy is reduced from  $1.15 \,\mathrm{J}\,\mathrm{m}^{-2}$  to  $1.0 \,\mathrm{J}\,\mathrm{m}^{-2}$ . As observed in Fig. 12(c) and (f), the crack has a stronger tendency to propagate along the grain boundary region with a reduced grain boundary cleavage energy. Whether it is possible to enforce the equivalence of the higher-order and multi-phase field models with the corresponding material parameters and degradation function is currently unknown, but will be examined in the future study.

Fig. 13 shows the Von Mises stress evolution within the unit cell. In this figure, 'MPF' stands for multi-phase-field, 'HPF' stands for high-order phase-field, and 'low GB' stands for reduced grain boundary cleavage energy. The stress–strain curves represent the evolution of homogenized Cauchy stress versus the axial strain in the tension direction. It is observed that the multi-phase-field generally has lower homogenized stress than the high-order phase-field in the elastic region. Two reasons may account for such observation. First, it has been argued in Fig. 4 that the second order phase-field has larger discretization error than high-order phase-field under the same mesh resolution. Also, such discretization error is further amplified when the elastic stiffness is determined by the combining effect of three phase fields. Therefore, the equivalent phase field is more distributed and the phase-field of the undamaged region is also larger than high-order phase-field, which results in more reduced elastic stiffness in multi-phase-field. A similar effect is observed in the Von Mises stress contour of multi-phase-field with intact grain boundary (Fig. 13 (a–c)) and with reduced grain boundary cleavage energy Fig. 13 (g–i). The stress distribution is relatively homogenized compared with typical crack tip stress field.

The accuracy of multi-phase-field might be increased with smaller regularization length scale  $l_0$  and more refined grid points. On the other hand, high-order phase-field offers higher accuracy under the same mesh resolution at the expense of higher computational cost. The phase field is less distributed within the unit cell, and stress relaxation region is observed besides the crack. Also, stress concentration is observed near the crack tip.

Another interesting aspect is that, when the grain boundary cleavage energy is reduced, the stress-strain response of the elastic region is not affected for both multi-phase-field and high-order phase-field. But the sudden-drop of

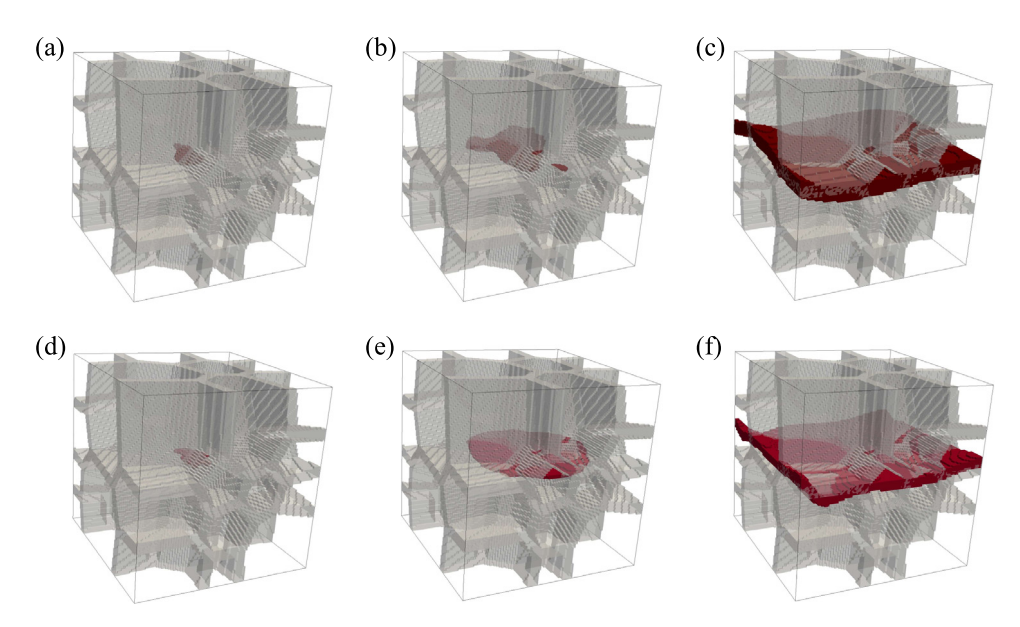


Fig. 11. Three-dimensional crack propagation in polycrystalline rock salt. (a-c) multi-phase-field case; (d-f) high-order phase-field case. The gray region corresponds to the grain boundary region, while the red region corresponds to the crack region. (For interpretation of the references to colour in this figure legend, the reader is referred to the web version of this article.)

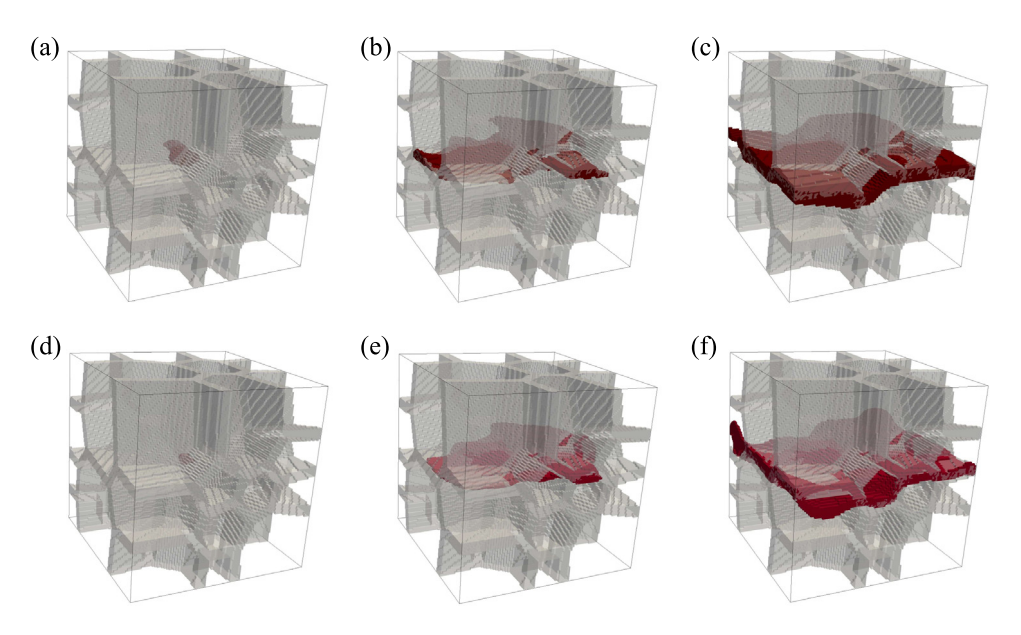


Fig. 12. Three-dimensional crack propagation in polycrystalline rock salt with reduced grain boundary cleavage energy. (a–c) multi-phase-field; (d-f) high-order phase-field. The gray region corresponds to the grain boundary region, while the red region corresponds to the crack region . (For interpretation of the references to colour in this figure legend, the reader is referred to the web version of this article.)

the load carrying ability occurs earlier, and crack has a larger possibility to propagate along the grain boundary (Fig. 12). Note that the stress within the cracked region can be further reduced by using lower residual stiffness k. Residual stiffness k as low as  $1.0 \times 10^{-6}$  has been used in FFT-based method [58] without introducing convergence issue typically observed in FFT-based method with sharp material contrast.

Finally, it should be noted that FFT solver is not the only feasible method that leverages the Green's function to accelerate simulations of polycrystals. For instance, Zhang and Oskay [90] have established a reduced-order

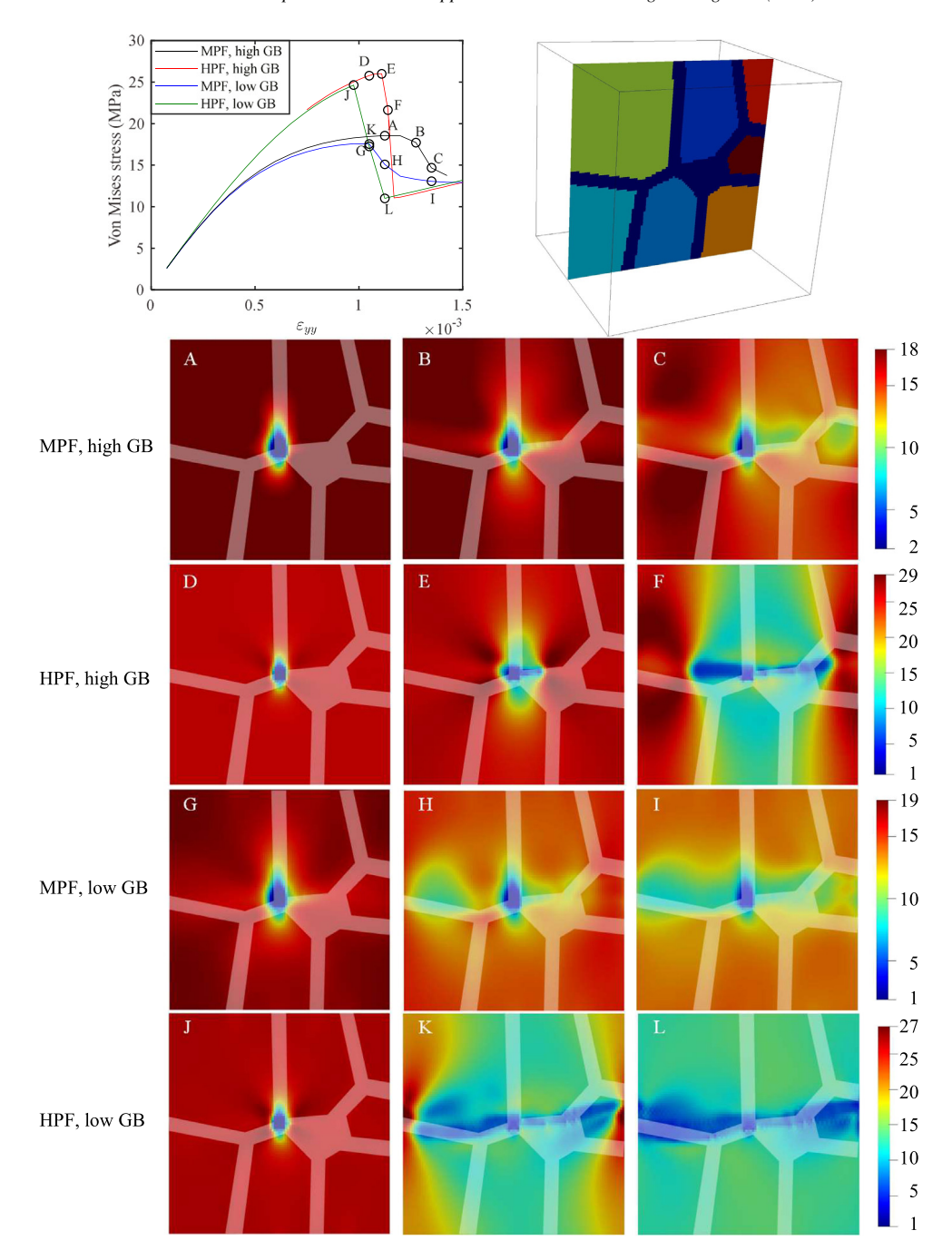


Fig. 13. Von Mises stress (in MPa) of the mid-plane of the RVE evolving during the tension test, where 'mpf' stands for multi-phase-field, 'hpf' stands for high-order phase-field, and 'gb' stands for reduced grain boundary cleavage energy. (a–c) Multi-phase-field; (d–f) High-order phase-field; (g–i) Multi-phase-field with reduced grain boundary cleavage energy; (j–l) High-order phase-field with reduced grain boundary cleavage energy.

multiscale homogenization procedure based on eigenstrain that is both sparse and scalable. The comparison among different approaches to accelerate simulations of fracture is an important topic, and will be considered in future studies.

#### 4. Conclusion

We introduce an FFT-based solver to solve the two most commonly used strongly anisotropic phase field fracture models, i.e., the multi-phase-field and high-order phase-field models in a periodic cell. The governing equations of both methods are derived in a periodic unit cell originated from the same total potential  $\Psi$ . Since Dirichlet boundary condition cannot be explicitly imposed in the FFT domain, a penalty term is added to the total potential  $\Psi$  to enforce the phase field in the initial failure region. The discrete frequency vector is generalized to enable calculating second order and fourth order gradient, which is required to solve the phase field model using a collocation method. Three numerical examples are utilized to demonstrate the accuracy and numerical behavior of the FFT-based method in solving strongly anisotropic phase field. Major conclusions are summarized below:

- 1. The FFT-based method is capable of consistently solving both multi-phase-field and high-order phase-field governing equations. Upon each mesh refinement, the surface energy error of both methods decreases toward zero.
- 2. With the same mesh resolution, the high-order phase-field model has lower surface energy error than the multi-phase-field counterpart.
- 3. No local perturbation or Gibbs phenomenon is observed in both cases even in the presence of the fourth-order gradient.
- 4. When the mesh resolution is sufficiently low, the FFT solvers for high-order phase-field and multi-phase-field models have similar computational costs. As mesh resolution increases, the high-order phase-field FFT solver requires much more linear solver iterations to converge to the same relative error.
- 5. When solved by FFT-based method, both multi-phase-field and high-order phase-field can represent sawtooth crack pattern typically observed in strongly anisotropic crack problem. Moreover, crack coalescence and branching are observed in three-dimensional polycrystalline microstructure.

Future work will target the following challenges. First, a more sophisticated preconditioner will be derived to improve the convergence rate of the linear solver. Currently, the condition number of the stiffness matrix increases with mesh resolution for both the multi-phase-field and high-order phase-field models. It is expected that a preconditioner or a Green's operator can be proposed such that the condition number can become independent of discretization. Second, the strongly anisotropic phase field method will be incorporated in a multiphysics framework for simulating the material behavior of polycrystalline rock salt at various temperature and strain rate. More specifically, the thermodynamic coupling of crystal plasticity [56], twinning [91], ductile fracture [16,82,92], solution-precipitation creep [93], and diffusion-controlled crack healing [94] will be addressed.

# Acknowledgments

The authors would like to thank Dr. Timothy Truster from the University of Tennessee for the fruitful discussion. The two anonymous reviewers have provided helpful suggestions and feedback that improve the manuscript. Their efforts are gratefully acknowledged. This research is supported by the Nuclear Energy University program from the Department of Energy under grant contract DE-NE0008534, the Earth Materials and Processes program from the US Army Research Office under grant contract W911NF-18-2-0306, the Dynamic Materials and Interactions Program from the Air Force Office of Scientific Research under grant contract FA9550-17-1-0169, as well as the Mechanics of Materials and Structures program at National Science Foundation, USA under grant contract CMMI-1462760 and the NSF CAREER grant CMMI-1846875. These supports are gratefully acknowledged. The views and conclusions contained in this document are those of the authors, and should not be interpreted as representing the official policies, either expressed or implied, of the sponsors, including the Army Research Laboratory or the U.S. Government. The U.S. Government is authorized to reproduce and distribute reprints for government purposes notwithstanding any copyright notation herein.

#### References

- [1] Gilles A. Francfort, J.-J. Marigo, Revisiting brittle fracture as an energy minimization problem, J. Mech. Phys. Solids 46 (8) (1998) 1319–1342.
- [2] Blaise Bourdin, Gilles A. Francfort, Jean-Jacques Marigo, The variational approach to fracture, J. Elasticity 91 (1-3) (2008) 5-148.
- [3] Christian Miehe, Fabian Welschinger, Martina Hofacker, Thermodynamically consistent phase-field models of fracture: variational principles and multi-field FE implementations, Internat. J. Numer. Methods Engrg. 83 (10) (2010) 1273–1311.

- [4] Sanghyun Lee, Mary F. Wheeler, Thomas Wick, Pressure and fluid-driven fracture propagation in porous media using an adaptive finite element phase field model, Comput. Methods Appl. Mech. Engrg. 305 (2016) 111–132.
- [5] Kun Wang, WaiChing Sun, A unified variational eigen-erosion framework for interacting brittle fractures and compaction bands in fluid-infiltrating porous media, Comput. Methods Appl. Mech. Engrg. 318 (2017) 1–32.
- [6] SeonHong Na, WaiChing Sun, Mathew D. Ingraham, Hongkyu Yoon, Effects of spatial heterogeneity and material anisotropy on the fracture pattern and macroscopic effective toughness of Mancos Shale in Brazilian tests, J. Geophys. Res. 122 (8) (2017) 6202–6230.
- [7] SeonHong Na, WaiChing Sun, Computational thermomechanics of crystalline rock, Part I: A combined multi-phase-field/crystal plasticity approach for single crystal simulations, Comput. Methods Appl. Mech. Engrg. 338 (2018) 657–691.
- [8] Rudy J.M. Geelen, Yingjie Liu, John E. Dolbow, Antonio Rodríguez-Ferran, An optimization-based phase-field method for continuous-discontinuous crack propagation, Internat. J. Numer. Methods Engrg. 116 (1) (2018) 1–20.
- [9] Eric C. Bryant, WaiChing Sun, A mixed-mode phase field fracture model in anisotropic rocks with consistent kinematics, Comput. Methods Appl. Mech. Engrg. 342 (2018) 561–584.
- [10] Jinhyun Choo, WaiChing Sun, Cracking and damage from crystallization in pores: Coupled chemo-hydro-mechanics and phase-field modeling, Comput. Methods Appl. Mech. Engrg. 335 (2018) 347–379.
- [11] José Reinoso, Marco Paggi, Christian Linder, Phase field modeling of brittle fracture for enhanced assumed strain shells at large deformations: formulation and finite element implementation, Comput. Mech. 59 (6) (2017) 981–1001.
- [12] Nima Noii, Fadi Aldakheel, Thomas Wick, Peter Wriggers, An adaptive global-local approach for phase-field modeling of anisotropic brittle fracture, 2019, ArXiv preprint, arXiv:1905.07519.
- [13] Yousef Heider, WaiChing Sun, A phase field framework for capillary-induced fracture in unsaturated porous media: drying-induced vs. hydraulic cracking, Comput. Methods Appl. Mech. Engrg. (2019).
- [14] Michael J. Borden, Thomas J.R. Hughes, Chad M. Landis, Clemens V. Verhoosel, A higher-order phase-field model for brittle fracture: Formulation and analysis within the isogeometric analysis framework, Comput. Methods Appl. Mech. Engrg. 273 (2014) 100–118b.
- [15] Michael J. Borden, Thomas J.R. Hughes, Chad M. Landis, Amin Anvari, Isaac J. Lee, A phase-field formulation for fracture in ductile materials: Finite deformation balance law derivation, plastic degradation, and stress triaxiality effects, Comput. Methods Appl. Mech. Engrg. 312 (2016) 130–166.
- [16] Jinhyun Choo, WaiChing Sun, Coupled phase-field and plasticity modeling of geological materials: from brittle fracture to ductile flow, Comput. Methods Appl. Mech. Engrg. 330 (2018) 1–32.
- [17] Richard A. Regueiro, Ronaldo I. Borja, Plane strain finite element analysis of pressure sensitive plasticity with strong discontinuity, Int. J. Solids Struct. 38 (21) (2001) 3647–3672.
- [18] Kun Wang, WaiChing Sun, A multiscale multi-permeability poroplasticity model linked by recursive homogenizations and deep learning, Comput. Methods Appl. Mech. Engrg. 334 (2018) 337–380.
- [19] Kun Wang, WaiChing Sun, Meta-modeling game for deriving theory-consistent, microstructure-based traction–separation laws via deep reinforcement learning, Comput. Methods Appl. Mech. Engrg. 346 (2019) 216–241.
- [20] Kun Wang, WaiChing Sun, An updated Lagrangian LBM-DEM-FEM coupling model for dual-permeability fissured porous media with embedded discontinuities, Comput. Methods Appl. Mech. Engrg. 344 (2019) 276–305.
- [21] Nicolas Moës, John Dolbow, Ted Belytschko, A finite element method for crack growth without remeshing, Internat. J. Numer. Methods Engrg. 46 (1) (1999) 131–150.
- [22] C. Armando Duarte, Ivo Babuška, J. Tinsley Oden, Generalized finite element methods for three-dimensional structural mechanics problems, Comput. Struct. 77 (2) (2000) 215–232.
- [23] WaiChing Sun, Zhijun Cai, Jinhyun Choo, Mixed Arlequin Method for multiscale poromechanics problems, Internat. J. Numer. Methods Engrg. 111 (7) (2017) 624–659.
- [24] Michael Ortiz, Anna Pandolfi, Finite-deformation irreversible cohesive elements for three-dimensional crack-propagation analysis, Internat. J. Numer. Methods Engrg. 44 (9) (1999) 1267–1282.
- [25] Christian Linder, Arun Raina, A strong discontinuity approach on multiple levels to model solids at failure, Comput. Methods Appl. Mech. Engrg. 253 (2013) 558–583.
- [26] Raúl Radovitzky, Andrew Seagraves, Mike Tupek, Ludovic Noels, A scalable 3D fracture and fragmentation algorithm based on a hybrid, discontinuous Galerkin, cohesive element method, Comput. Methods Appl. Mech. Engrg. 200 (1–4) (2011) 326–344.
- [27] J.D. Clayton, J. Knap, Phase field modeling of directional fracture in anisotropic polycrystals, Comput. Mater. Sci. 98 (2015) 158–169.
- [28] A. Quintanas-Corominas, J. Reinoso, E. Casoni, A. Turon, J.A. Mayugo, A phase field approach to simulate intralaminar and translaminar fracture in long fiber composite materials, Compos. Struct. 220 (2019) 899–911.
- [29] Thanh-Tung Nguyen, Julien Rethore, Julien Yvonnet, Marie-Christine Baietto, Multi-phase-field modeling of anisotropic crack propagation for polycrystalline materials, Comput. Mech. 60 (2) (2017) 289–314.
- [30] Jeremy Bleyer, Roberto Alessi, Phase-field modeling of anisotropic brittle fracture including several damage mechanisms, Comput. Methods Appl. Mech. Engrg. 336 (2018) 213–236.
- [31] S. Teichtmeister, D. Kienle, F. Aldakheel, M.-A. Keip, Phase field modeling of fracture in anisotropic brittle solids, Int. J. Non-Linear Mech. 97 (2017) 1–21.
- [32] Thomas J.R. Hughes, John A. Cottrell, Yuri Bazilevs, Isogeometric analysis: CAD, finite elements, NURBS, exact geometry and mesh refinement, Comput. Methods Appl. Mech. Engrg. 194 (39–41) (2005) 4135–4195.
- [33] Héctor Gómez, Victor M. Calo, Yuri Bazilevs, Thomas J.R. Hughes, Isogeometric analysis of the Cahn-Hilliard phase-field model, Comput. Methods Appl. Mech. Engrg. 197 (49–50) (2008) 4333–4352.
- [34] H. Moulinec, P. Suquet, A fast numerical method for computing the linear and nonlinear mechanical properties of composites, C. R. Acad. Sci. II 318 (11) (1994) 1417–1423.

- [35] Sébastien Brisard, Overview of FFT-based homogenization techniques from the Galerkin point of view, in: Conférence Internationale de Géotechnique, Des Ouvrages Et Structures, CIGOS 2015, 2015.
- [36] Frédéric Feyel, A multilevel finite element method (FE2) to describe the response of highly non-linear structures using generalized continua, Comput. Methods Appl. Mech. Eng. 192 (28–30) (2003) 3233–3244.
- [37] WaiChing Sun, José E. Andrade, John W. Rudnicki, Peter Eichhubl, Connecting microstructural attributes and permeability from 3D tomographic images of in situ shear-enhanced compaction bands using multiscale computations, Geophys. Res. Lett. 38 (10) (2011).
- [38] Wai Ching Sun, Jose E. Andrade, John W. Rudnicki, Multiscale method for characterization of porous microstructures and their impact on macroscopic effective permeability, Internat. J. Numer. Methods Engrg. 88 (12) (2011) 1260–1279.
- [39] Yang Liu, WaiChing Sun, Zifeng Yuan, Jacob Fish, A nonlocal multiscale discrete-continuum model for predicting mechanical behavior of granular materials, Internat. J. Numer. Methods Engrg. 106 (2) (2016) 129–160.
- [40] Ghassan Shahin, Jacques Desrues, Stefano Dal Pont, Gaël Combe, Albert Argilaga, A study of the influence of REV variability in double-scale FEM× DEM analysis, Internat. J. Numer. Methods Engrg. 107 (10) (2016) 882–900.
- [41] Ling Wu, Ludovic Noels, L. Adam, Issam Doghri, A multiscale mean-field homogenization method for fiber-reinforced composites with gradient-enhanced damage models, Comput. Methods Appl. Mech. Engrg. 233 (2012) 164–179.
- [42] H. Moulinec, P. Suquet, A numerical method for computing the overall response of nonlinear composites with complex microstructure, Comput. Methods Appl. Mech. Engrg. 157 (1–2) (1998) 69–94.
- [43] David J. Eyre, Graeme W. Milton, A fast numerical scheme for computing the response of composites using grid refinement, Eur. Phys. J. Appl. Phys. (ISSN: 1286-0042) 6 (1) (1999) 41–47.
- [44] J.C. Michel, H. Moulinec, P. Suquet, Effective properties of composite materials with periodic microstructure: a computational approach, Comput. Methods Appl. Mech. Engrg. (ISSN: 0045-7825) 172 (1) (1999) 109–143.
- [45] Ricardo A. Lebensohn, N-site modeling of a 3D viscoplastic polycrystal using fast fourier transform, Acta Mater. 49 (14) (2001) 2723–2737.
- [46] A. Prakash, R.A. Lebensohn, Simulation of micromechanical behavior of polycrystals: finite elements versus fast Fourier transforms, Modelling Simulation Mater. Sci. Eng. 17 (6) (2009) 064010.
- [47] Ran Ma, Timothy J. Truster, FFT-Based homogenization of hypoelastic plasticity at finite strains, Comput. Methods Appl. Mech. Engrg. (2019).
- [48] F. Roters, P. Eisenlohr, L. Hantcherli, D.D. Tjahjanto, T.R. Bieler, D. Raabe, Overview of constitutive laws, kinematics, homogenization and multiscale methods in crystal plasticity finite-element modeling: Theory, experiments, applications, Acta Mater. (ISSN: 1359-6454) 58 (4) (2010) 1152–1211.
- [49] Jia Li, Xiao-Xiao Tian, Radhi Abdelmoula, A damage model for crack prediction in brittle and quasi-brittle materials solved by the FFT method, Int. J. Fracture 173 (2) (2012) 135–146.
- [50] Martin Boeff, Florian Gutknecht, Philipp S. Engels, Anxin Ma, Alexander Hartmaier, Formulation of nonlocal damage models based on spectral methods for application to complex microstructures, Eng. Fract. Mech. 147 (2015) 373–387.
- [51] Bing Wang, Guodong Fang, Shuo Liu, Maoqing Fu, Jun Liang, Progressive damage analysis of 3D braided composites using FFT-based method, Compos. Struct. 192 (2018) 255–263.
- [52] Luv Sharma, Ron H.J. Peerlings, Pratheek Shanthraj, Franz Roters, Marc G.D. Geers, FFT-Based interface decohesion modelling by a nonlocal interphase, Adv. Model. Simul. Eng. Sci. 5 (1) (2018) 7.
- [53] J. Spahn, H. Andrä, M. Kabel, R. Müller, A multiscale approach for modeling progressive damage of composite materials using fast fourier transforms, Comput. Methods Appl. Mech. Engrg. 268 (2014) 871–883.
- [54] Andrea Rovinelli, Henry Proudhon, Ricardo A. Lebensohn, Michael D. Sangid, Assessing the reliability of fast fourier transform-based crystal plasticity simulations of a polycrystalline material near a crack tip, Int. J. Solids Struct. (2019).
- [55] Long Qing Chen, Jie Shen, Applications of semi-implicit fourier-spectral method to phase field equations, Comput. Phys. Comm. 108 (2–3) (1998) 147–158.
- [56] L. Chen, J. Chen, R.A. Lebensohn, Y.Z. Ji, T.W. Heo, S. Bhattacharyya, K. Chang, S. Mathaudhu, Z.K. Liu, L.-Q. Chen, An integrated fast fourier transform-based phase-field and crystal plasticity approach to model recrystallization of three dimensional polycrystals, Comput. Methods Appl. Mech. Engrg. 285 (2015) 829–848.
- [57] Julian Kochmann, Stephan Wulfinghoff, Stefanie Reese, Jaber Rezaei Mianroodi, Bob Svendsen, Two-scale FE-FFT-and phase-field-based computational modeling of bulk microstructural evolution and macroscopic material behavior, Comput. Methods Appl. Mech. Engrg. 305 (2016) 89–110.
- [58] Yang Chen, Dmytro Vasiukov, Lionel Gélébart, Chung Hae Park, A FFT solver for variational phase-field modeling of brittle fracture, Comput. Methods Appl. Mech. Engrg. 349 (2019) 167–190.
- [59] Franz Roters, Martin Diehl, Pratheek Shanthraj, Philip Eisenlohr, C. Reuber, Su Leen Wong, Tias Maiti, Alireza Ebrahimi, Thomas Hochrainer, H.-O. Fabritius, et al., DAMASK-The Düsseldorf Advanced Material Simulation Kit for modeling multi-physics crystal plasticity, thermal, and damage phenomena from the single crystal up to the component scale, Comput. Mater. Sci. 158 (2019) 420–478.
- [60] Jan Zeman, Jaroslav Vondřejc, Jan Novák, Ivo Marek, Accelerating a FFT-based solver for numerical homogenization of periodic media by conjugate gradients, J. Comput. Phys. 229 (21) (2010) 8065–8071.
- [61] Stéphane Berbenni, Vincent Taupin, Komlan Sénam Djaka, Claude Fressengeas, A numerical spectral approach for solving elasto-static field dislocation and g-disclination mechanics, Int. J. Solids Struct. 51 (23–24) (2014) 4157–4175.
- [62] François Willot, Bassam Abdallah, Yves-Patrick Pellegrini, Fourier-based schemes with modified green operator for computing the electrical response of heterogeneous media with accurate local fields, Internat. J. Numer. Methods Engrg. 98 (7) (2014) 518–533.
- [63] Matti Schneider, Felix Ospald, Matthias Kabel, Computational homogenization of elasticity on a staggered grid, Internat. J. Numer. Methods Engrg. 105 (9) (2016) 693–720.

- [64] SeonHong Na, WaiChing Sun, A multi-phase-field anisotropic damage-plasticity model for crystalline rocks, in: Proceedings of China-Europe Conference on Geotechnical Engineering, Springer, 2018, pp. 57–60.
- [65] Adnan Eghtesad, Miroslav Zecevic, Ricardo A. Lebensohn, Rodney J. McCabe, Marko Knezevic, Spectral database constitutive representation within a spectral micromechanical solver for computationally efficient polycrystal plasticity modelling, Comput. Mech. 61 (1–2) (2018) 89–104.
- [66] T.I. Zohdi, P. Wriggers, Aspects of the computational testing of the mechanical properties of microheterogeneous material samples, Internat. J. Numer. Methods Engrg. 50 (11) (2001) 2573–2599.
- [67] Jacob Fish, Practical Multiscaling, John Wiley & Sons, 2013.
- [68] Kun Wang, WaiChing Sun, Anisotropy of a tensorial bishop's coefficient for wetted granular materials, J. Eng. Mech. 143 (3) (2015) B4015004.
- [69] WaiChing Sun, Matthew R. Kuhn, John W. Rudnicki, A multiscale DEM-LBM analysis on permeability evolutions inside a dilatant shear band, Acta Geotech. 8 (5) (2013) 465–480.
- [70] Christian Miehe, Fabian Welschinger, Martina Hofacker, Thermodynamically consistent phase-field models of fracture: variational principles and multi-field FE implementations, Internat. J. Numer. Methods Engrg. 83 (10) (2010) 1273–1311.
- [71] Aurel Qinami, Eric Cushman Bryant, WaiChing Sun, Michael Kaliske, Circumventing mesh bias by r-and h-adaptive techniques for variational eigenfracture, Int. J. Fract. (2019) 1–14.
- [72] John D. Clayton, Nonlinear Mechanics of Crystals, vol. 177, Springer Science & Business Media, 2010.
- [73] Lei Liu, Yan Bi, Jian Xu, Xiangrong Chen, Ab initio study of the elastic properties of sodium chloride at high pressure, Physica B 405 (9) (2010) 2175–2180.
- [74] K.H. Pham, K. Ravi-Chandar, C.M. Landis, Experimental validation of a phase-field model for fracture, Int. J. Fract. 205 (1) (2017) 83–101.
- [75] Jan Zeman, Tom W.J. de Geus, Jaroslav Vondřejc, Ron H.J. Peerlings, Marc G.D. Geers, A finite element perspective on nonlinear FFT-based micromechanical simulations, Internat. J. Numer. Methods Engrg. 111 (10) (2017) 903–926.
- [76] Katerina E. Aifantis, J.R. Willis, The role of interfaces in enhancing the yield strength of composites and polycrystals, J. Mech. Phys. Solids 53 (5) (2005) 1047–1070.
- [77] Clemens V. Verhoosel, René de Borst, A phase-field model for cohesive fracture, Internat. J. Numer. Methods Engrg. 96 (1) (2013) 43–62.
- [78] Marco Paggi, Mauro Corrado, José Reinoso, Fracture of solar-grade anisotropic polycrystalline silicon: A combined phase field–cohesive zone model approach, Comput. Methods Appl. Mech. Engrg. 330 (2018) 123–148.
- [79] Bin Li, Corrado Maurini, Crack kinking in a variational phase-field model of brittle fracture with strongly anisotropic surface energy, J. Mech. Phys. Solids 125 (2019) 502–522.
- [80] Félix Mouhat, François-Xavier Coudert, Necessary and sufficient elastic stability conditions in various crystal systems, Phys. Rev. B 90 (22) (2014) 224104.
- [81] Mary F. Wheeler, T. Wick, W. Wollner, An augmented-Lagrangian method for the phase-field approach for pressurized fractures, Comput. Methods Appl. Mech. Engrg. 271 (2014) 69–85.
- [82] Christian Miehe, Fadi Aldakheel, Arun Raina, Phase field modeling of ductile fracture at finite strains: A variational gradient-extended plasticity-damage theory, Int. J. Plast. 84 (2016) 1–32.
- [83] Marreddy Ambati, Tymofiy Gerasimov, Laura De Lorenzis, A review on phase-field models of brittle fracture and a new fast hybrid formulation, Comput. Mech. 55 (2) (2015) 383–405.
- [84] A. Yuse, M. Sano, Transition between crack patterns in quenched glass plates, Nature 362 (6418) (1993) 329.
- [85] Atsushi Takei, Benoît Roman, José Bico, Eugenio Hamm, Francisco Melo, Forbidden directions for the fracture of thin anisotropic sheets: an analogy with the wulff plot, Phys. Rev. Lett. 110 (14) (2013) 144301.
- [86] Bin Li, Christian Peco, Daniel Millán, Irene Arias, Marino Arroyo, Phase-field modeling and simulation of fracture in brittle materials with strongly anisotropic surface energy, Internat. J. Numer. Methods Engrg. 102 (3–4) (2015) 711–727.
- [87] Michael J. Borden, Thomas J.R. Hughes, Chad M. Landis, Clemens V. Verhoosel, A higher-order phase-field model for brittle fracture: Formulation and analysis within the isogeometric analysis framework, Comput. Methods Appl. Mech. Engrg. 273 (2014) 100–118a.
- [88] R. Quey, P.R. Dawson, F. Barbe, Large-scale 3D random polycrystals for the finite element method: Generation, meshing and remeshing, Comput. Methods Appl. Mech. Engrg. (ISSN: 0045-7825) 200 (17–20) (2011) 1729–1745.
- [89] Yujie Wei, Lallit Anand, On micro-cracking, inelastic dilatancy, and the brittle-ductile transition in compact rocks: A micro-mechanical study, Int. J. Solids Struct. 45 (10) (2008) 2785–2798.
- [90] Xiang Zhang, Caglar Oskay, Sparse and scalable eigenstrain-based reduced order homogenization models for polycrystal plasticity, Comput. Methods Appl. Mech. Engrg. 326 (2017) 241–269.
- [91] John D. Clayton, Jarek Knap, A phase field model of deformation twinning: nonlinear theory and numerical simulations, Physica D 240 (9–10) (2011) 841–858.
- [92] Clemens V. Verhoosel, René de Borst, A phase-field model for cohesive fracture, Internat. J. Numer. Methods Engrg. 96 (1) (2013) 43–62.
- [93] Janos L. Urai, Christopher J. Spiers, Hendrik J. Zwart, Gordon S. Lister, Weakening of rock salt by water during long-term creep, Nature 324 (6097) (1986) 554.
- [94] J.L. Urai, Z. Schléder, C.J. Spiers, P.A. Kukla, Flow and transport properties of salt rocks, Dyn. Complex Intracontinental Basins (2008) 277-290.